

Title: Inclusion Removal by Bubble Flotation in a Continuous Casting Mold

Authors:

Lifeng Zhang, Jun Aoki, Brian G. Thomas

University of Illinois at Urbana-Champaign, 1206 W. Green St., Urbana, IL 61801, USA

Phone number: 1-217-244-4656, Fax number: 1-217-244-6534

Email: zhang25@uiuc.edu, bgthomas@uiuc.edu

Correspondence author:

Dr. Lifeng Zhang

Research Scientist,

Department of Mechanical & Industrial Engineering

University of Illinois at Urbana-Champaign

MEB345, MC244, 1206 W. Green St., Urbana, IL 61801, USA

Phone number: 1-217-244-4656, Fax number: 1-217-244-6534

Email: zhang25@uiuc.edu

Abstract

Fundamentally-based computational models are developed and applied to quantify the removal of inclusions by bubbles during the continuous casting of steel. First, the attachment probability of inclusions on a bubble surface is investigated based on fundamental fluid flow simulations, incorporating the turbulent inclusion trajectory and sliding time of each individual inclusion along the bubble surface as a function of particle and bubble size. Then, the turbulent fluid flow in a typical continuous casting mold, trajectories of bubbles and their path length in the mold are calculated. The change in inclusion distribution due to removal by bubble transport in the mold is calculated based on the computed attachment probability of inclusions on each bubble and the computed path length of the bubbles. In addition to quantifying inclusion removal for many different cases, the results are important to evaluate the significance of different inclusion removal mechanisms. The modeling approach presented here is a powerful tool for investigating multi-scale phenomena in steelmaking and casting operations, in order to learn how to optimize conditions to lower defects.

Keywords: Inclusion Removal, Bubble Flotation, Continuous Casting Mold, Attachment Probability

I. INTRODUCTION

Non-metallic inclusions in molten steel can lead to serious defects in the final product, and the continuous casting process is the last chance to remove them. Gas injection is commonly applied to many secondary metallurgical processes such as ladle treatment, RH degassing, and Submerged Entry Nozzles (SEN). Although it is well-known that gas injection helps to remove inclusions, the mechanisms and removal rates have not been quantified. This work presents fundamental models to quantify the removal of inclusions by bubbles in molten steel and applies them to the continuous casting mold for typical conditions. The problem of modeling the multiple size and time scales involved in inclusion removal by bubbles is handled by separating the phenomena into models at two different scales. A small-scale model is used to quantify the attachment probability of individual inclusions to individual bubbles. The results used in a large-scale coupled model of turbulent fluid flow in the entire metallurgical vessel, including the transport of bubbles and inclusions. After briefly reviewing previous work on five relevant topics, the models and corresponding results are presented in three sections: 1) fundamental inclusion - bubble interactions and attachment probabilities, 2) bubble trajectories and 3) inclusion removal.

II. INCLUSION ATTACHMENT TO BUBBLES IN MOLTEN STEEL

A. *Defects*

Gas injection processes in steel refining focus on achieving two conditions: fine bubbles and good mixing. ^[1-6] During steel secondary refining, finer bubbles provide larger gas/liquid interfacial area and higher attachment probability of inclusions to bubbles ^[3, 6]. Good mixing enhances the efficiency of the transfer of the alloy elements. Bubbles injected into the SEN and continuous casting mold affect steel quality in several ways:

- Helping to reduce nozzle clogging;
- Influencing the flow pattern in the mold;
- Generating top surface level fluctuations and even slag emulsification if the gas flow rate is too large;
- Capturing inclusions moving within the molten steel, agglomerating them, and removing some of them into the top slag. ^[3, 7-9]

- Entrapping bubbles and inclusion clusters into the solidified shell, eventually leading to line defects such as surface slivers, blisters, pencil pipes or internal defects in the rolled product.^[7, 8, 10-12]

Aided by surface tension forces from nonwetting contact, most solid inclusions tend to collect on surfaces such as bubbles, as shown in **Figure 1**^[13, 14]. Line defects on the surface of finished strip products, are several tens of micrometers to millimeter in width and as long as 0.1-1 meter^[15]. Serious “sliver” defects result from clusters of nonmetallic inclusions caught near the surface of the slab (<15mm from the surface). If the surface defects contain bubbles, they are called “pencil pipe”, blow holes, blisters^[15], or pores. After rolling of low-strength steels for exposed automotive applications, for example, the bubbles are elongated, and during annealing, gas expansion can generate internal pressure that raises the surface, creating an ugly surface streak. This tubular shape surface defect has a smooth slightly raised surface, typically ~1mm wide and 150-300mm long^[15, 16], as shown in **Figure 2**^[15, 17].

B. *Inclusion Attachment Probability*

The process of inclusion removal by gas bubbles is characterized by the attachment probability. This process is influenced by many factors including the turbulent fluid flow of the molten steel, the shape and size of both bubbles and inclusions, surface tension effects, and bubble removal rates, which are affected by slag properties. The attachment probability is the fraction of inclusions that pass the rising bubble and attach to it. When turbulence levels are small, it can be defined as follows:

$$P = \frac{N_o}{N_T} = \left(\frac{d_{os}}{d_B + 2d_p} \right)^2, \quad (1)$$

where N_o is the number of inclusions attaching to the bubble, and N_T is the number of inclusions in the column of fluid swept by the moving bubble with diameter $d_B + 2d_p$. Without the stochastic effect of turbulence, only particles starting within a critical distance from the bubble axis d_{os} will be entrapped, as shown in **Figure 3a**.

W.Pan et al measured the removal of particles (100~800μm in size) by bubble flotation in a water model by analyzing high speed camera photos.^[1] Zhang and Taniguchi studied inclusion

removal by bubble flotation in a water model under turbulent conditions by measuring the particle number density, i.e. size distribution, using a Coulter Counter .^[6]

Several papers model the contribution of turbulence to the attachment of inclusions to bubbles in water system in terms of turbulent energy dissipation rate. Schubert ^[18] reported that the attachment probability P is related to the bubble size (d_B), particle size (d_p), and turbulent energy dissipation rate (ε) by $P \propto \varepsilon^{4/9} \left[(C_1 d_p^{7/9})^2 + (C_2 d_B^{7/9})^2 \right]^{1/2}$, if $d_p, d_B \geq 15(\nu^3/\varepsilon)^{1/4}$. For metallurgical melts, the typical value of ε is $0.0001-1\text{m}^2/\text{s}^3$, so this equation can be used only if $d_p, d_B \geq 458\mu\text{m}$. Zhang et al ^[6] derived the attachment probability to be $P \propto (d_p/d_B)^{2.65} \varepsilon^{0.104} Q_g^{1.630}$, where Q_g is the gas flow rate. Zhang discussed the fundamentals of inclusion removal by bubble flotation in molten steel under laminar flow conditions and tentatively discussed the effect of turbulence; ^[3] A.G.Szekely investigated the removal of solid particles from molten aluminum during the spinning nozzle flotation process; ^[19] K.Okumura et al studied the removal of SiO_2 inclusions from molten Cu to the slag under gas injection stirring conditions; ^[20] Y.Miki et al investigated inclusion removal during steel RH degassing considering bubble flotation as one of the inclusion removal methods ^[21].

C: *Inclusion-Bubble Interaction*

The process of attaching an inclusion to a gas bubble in molten steel proceeds through the following steps. First, the inclusion approaches the gas bubble, and collides if it gets close enough. If the thin film of liquid between the particle and the bubble decreases to less than a critical thickness, it will suddenly rupture causing the inclusion to attach permanently to the surface of the bubble during the collision. Otherwise, if it slides along the surface of the bubble for a long enough time, the thin film can drain away and rupture, again leading to inclusion attachment. Otherwise, the inclusion will move away and detach from the bubble.

The interaction time between the bubble and the inclusion, t_i , includes the time while the inclusion collides with the bubble (collision time) and possibly also the time where it slides across its surface (sliding time). The collision time, t_c , starts with the deformation of the bubble by the inclusion and finishes at the instant of restoration of the bubble to its original size. Ye and Miller ^[22] give the collision time as Eq.(2)

$$t_c = \left(\frac{d_p^3 \rho_p}{12\sigma} \right)^{1/2} \quad (2)$$

where ρ_p is inclusion density (kg/m^3). The collision time depends mainly on the inclusion size, and is independent of the bubble size.

The film drainage time, t_F , is the time required for the drainage of the liquid film between the bubble and the inclusion until a critical film thickness is reached and rupture occurs. H.J.Schulze^[23] derived the rupture time of the film formed between a solid particle and a gas bubble,

$$t_F = \frac{3}{64} \mu \frac{\alpha^2}{k\sigma h_{Cr}^2} d_p^3 \quad (3)$$

where $k=4$. α is the angle (in rad) for the transition of the spherically deformed part of the bubble surface to the non-spherically deformed part, given by Eq(8)^[3]

$$\alpha = \arccos \left(1 - 1.02 \left(\frac{\pi d_p \rho_p u_B^2}{12\sigma} \right)^{1/2} \right) \quad (4)$$

where h_{Cr} is the critical thickness of liquid film for film rupture, given by^[3]

$$h_{Cr} = 2.33 \times 10^{-8} [1000\sigma(1 - \cos \theta)]^{0.16} \quad (5)$$

where θ is the contact angle of the inclusions at the bubble-steel interface.

After a particle has broken through the liquid film and reached the gas bubble, it will reside stably at gas/liquid interface regardless of the contact angle. Subsequent detachment is difficult, especially for particles that are small relative to the bubble size.

D. Bubble Size

Gas can be injected into the molten steel by various devices, such as tuyeres, lances, and porous refractory plugs, which govern the initial bubble size. Large bubbles can breakup according to the local turbulence level. The size of the largest surviving bubbles can be estimated by the forces imposed on the bubble.^[3] The average equivalent size of bubbles to survive the turbulence in secondary steel refining processes is predicted to be 10-20mm^[3, 24] and

~5mm in the CC mold ^[3]. Bubble shape changes with size. The aspect ratio of the bubble, e , varies according to the following empirical relationship, ^[25]

$$e = 1 + 0.163Eo^{0.757}, \quad (6)$$

where Eo is the Eötvös number, which represents the ratio between the buoyancy and surface tension forces

$$Eo = \frac{gd_B^2(\rho - \rho_g)}{\sigma}, \quad (7)$$

where g is the gravitational acceleration, d_B is bubble diameter, ρ and ρ_g are densities of the molten steel and the argon gas respectively, and σ is the surface tension of the molten steel. **Figure 4** shows the aspect ratio e of bubbles in molten steel, indicating that <3mm bubbles are spherical, 3-10mm bubbles are spheroidal, and >10mm bubble are spherical-cap shaped ^[26-28]. Most bubbles in the continuous casting mold are nearly spherical due to their size of ~5mm..

The shape of the bubble also depends on the ratio of the turbulent pressure fluctuation to the capillary pressure, which is related to the Weber number. If the bubble Weber number exceeds a critical value, the bubble will breakup. Thus, bubble size decreases with increasing stirring intensity of the liquid phase ^[3], according to ^[29]

$$d_{Bmax} \approx We_{Crit}^{0.6} \left(\frac{\sigma \times 10^3}{\rho \times 10^{-3}} \right)^{0.6} (\varepsilon \times 10)^{-0.4} \times 10^{-2} \quad (8)$$

where d_{Bmax} is the maximum bubble size in m; ε is the turbulent energy dissipation rate in W/t; σ is the surface tension in N/m ; ρ is the density of the molten steel in kg/m³ , and the critical Weber number $We_{Crit} \approx 0.59-1.3$. This relationship is shown in **Figure 5**. The stirring intensities of various metallurgical systems are also shown in this figure. ^[3] The highly turbulent flow in the SEN will break up any gas pockets into fine bubbles around 5mm in diameter. The newly-developed swirl SEN ^[30-33] may induce larger energy dissipation rate and generate much smaller bubbles.

E. Bubble Terminal Velocity

The terminal velocity of bubbles rising in molten steel is difficult to measure accurately. Density, viscosity and surface tension of the liquid affect the bubble terminal velocity as do bubble size and the turbulent fluid flow characteristics. **Figure 6** shows the terminal velocities of gas bubbles in the molten steel as calculated by different models ^[3]. A smoothed mean of the

bubble velocity predicted by these models is compared with the predictions of the model in the current work (presented later).

The terminal velocity of a bubble can be calculated from a force balance between the buoyancy force (F_B) and the drag force (F_D) acting on the bubble. The buoyancy force is expressed by

$$F_B = \frac{\pi d_B^3}{6} (\rho - \rho_g) \quad (9)$$

and the total drag force F_D is calculated by integrating over the surface of the bubble.

$$F_D = \int_S \tau_{ij} dA = \int_S \left[-p \delta_{ij} + \mu \left(\frac{\partial u_j}{\partial x_i} + \frac{\partial u_i}{\partial x_j} \right) \right] dA \quad (10)$$

where τ_{ij} is the total shear force on the portion of the bubble surface, p is the pressure, μ is the viscosity of the molten steel, u_i and u_j are the velocity components of the fluid flow, x_i and x_j are the coordinates, and δ_{ij} is the Kronecker delta, which equals zero if $i \neq j$, else equals unit.

The drag force depends on the size, velocity, and surface condition of the bubble, while the buoyancy force only depends on the bubble size. By applying $F_B = F_D$, for a given size bubble and surface condition, the terminal velocity of the bubble can be obtained. For a free bubble, a zero shear condition is the most appropriate boundary condition on the bubble surface. The alternative surface boundary condition of zero velocity, or called “no slip”, is more appropriate for bubbles with rigid surfaces, such as caused by surface-active elements or covering the surface with particles. Fig.6 shows that the terminal velocity of bubbles calculated with the zero shear surface condition agrees well with the mean of other analytical models. Thus the mean value of models 1-5 is used as the terminal velocity of bubbles when the fluid flow around bubbles is simulated. A peak occurs at a bubble diameter of 3 mm, where the bubble shape starts to change from spherical to ellipsoidal. Ellipsoidal bubbles (3-10 mm) have similar velocity. For bubbles larger than 10mm, terminal velocity increases rapidly with increasing size due to their spherical cap shape.

III. INCLUSION ATTACHMENT TO GAS BUBBLES

A. Model Formulation

In order to determine the interaction time and the attachment probability of inclusions to the bubble surface, a computational simulation of turbulent flow around an individual bubble and a

simulation of inclusion transport through the flow field were developed. First, the steady turbulent flow of molten steel around an argon bubble is calculated by solving the continuity equation, Navier-Stokes equations, and the standard equations for turbulent energy and its dissipation rate transport in two dimensions, assuming axi-symmetry. The domain included 15-20 times bubble diameter distance before and after the bubble using the finite differentiation code FLUENT.^[34] Possible deformation of the bubble shape by the flow and inclusion motion is ignored. The inlet velocity and far-field velocity condition are set to of the bubble terminal velocity, assuming a suitable turbulent energy and dissipation rate, and a far field pressure outlet.

Both zero-velocity and zero-shear stress boundary condition at the fluid-bubble interface were applied and the results were compared. The terminal velocities of bubbles were the mean value in Fig.6. The zero-velocity condition produces slightly lower velocities for small spherical bubbles and higher velocities for larger spherical bubbles. The zero-shear condition was assumed for the rest of the results in this work. The trajectory of each inclusion particle is then calculated from the computed velocity field by integrating the following particle velocity equation, which considers the balance between drag and buoyancy forces.

$$\frac{du_{pi}}{dt} = \frac{3}{4} \frac{1}{d_p} \frac{\rho}{\rho_p} C_D (u_{pi} - u_i)^2 - \frac{(\rho - \rho_p)}{\rho_p} g_i \quad (11)$$

where $u_{p,i}$ is the particle velocity, m/s; and C_D , is the drag coefficient given below as a function of particle Reynolds number (Re_p),

$$C_D = \frac{24}{Re_p} (1 + 0.186 Re_p^{0.653}) \quad (12)$$

To incorporate the “stochastic” effect of turbulent fluctuations on the particle motion, this work uses the “random walk” model in FLUENT.^[35] In this model, particle velocity fluctuations are based on a Gaussian-distributed random number, chosen according to the local turbulent kinetic energy. The random number is changed, thus producing a new instantaneous velocity fluctuation, at a frequency equal to the characteristic lifetime of the eddy. The instantaneous fluid velocity is then given by

$$u = \bar{u} + u' \quad (13)$$

$$u' = \xi \sqrt{u'^2} = \xi \sqrt{2k/3} \quad (14)$$

where u is the instantaneous fluid velocity, m/s; \bar{u} is the mean fluid phase velocity, m/s; u' is random velocity fluctuation, m/s; ξ is the random number, and k is the local level of turbulent kinetic energy in m^2/s^3 .

As boundary conditions, inclusions reflect if they touch the surface of the bubble. Attachment between the inclusion and the bubble was determined by the following steps. If the normal distance from the inclusion center to the surface of the bubble quickly becomes less than the inclusion radius, then collision attachment takes place. This was rare. Then, the interaction time between the bubble and the inclusion, t_I , is calculated from the inclusion centerline trajectory results by tracking the sliding time that elapses while the distance from the inclusion center to the surface of the bubble is less than the inclusion radius. Then, if $t_I > t_F$, the inclusion will be attached to the surface of the bubble.

The attachment probability is then calculated using Eq.(1) by injecting several thousand inclusions uniformly with the local velocity into the domain in a column with diameter $d_B + 2d_p$ for non-stochastic cases.

The classic attachment probability schematic, given in Fig.3a does not apply in turbulent conditions. Due to the stochastic effect of turbulence, some inclusions inside the column of d_{OS} may not interact with the bubble. On the other hand, other inclusions even far outside the column $d_B + 2d_p$ may interact, collide and attach onto the bubble surface. To model this effect, inclusions were injected into a column that was 15-20 times of the bubble diameter in order to compute this accurately. Then the attached probability, as shown in **Figure 3b**, was obtained by

$$P = \frac{\sum_i P_i A_i}{A_{B+2P}} = \frac{\sum_i \left[\frac{N_{o,i}}{N_{T,i}} \left(\pi(R_i + \Delta R)^2 - \pi R_i^2 \right) \right]}{\frac{\pi(d_B + 2d_p)^2}{4}}, \quad (15)$$

where N_o is the number of inclusions attaching to the bubble by satisfying either $t_I > t_F$, A_{B+2P} is the cross section area of the column with diameter of $d_B + 2d_p$. N_{Ti} is the total number of inclusions injected through the area A_i , and i is the number of the annular area at which the inclusions are injected.

In the current investigation, the following parameters are used: $\rho=7020 \text{ kg/m}^3$, $\rho_p=2800 \text{ kg/m}^3$, $\rho_g=1.6228 \text{ kg/m}^3$, $\sigma=1.40 \text{ N/m}$, $\theta=112^\circ$, $\mu=0.0067 \text{ kg/m-s}$, $d_p=1\text{-}100\mu\text{m}$, and $d_B=1\text{-}10\text{mm}$. These parameters represent typical spherical solid inclusions such as alumina in molten steel.

B. *Fluid Flow and Inclusion Motion Around a Bubble*

Figure 7 shows the fluid flow pattern behind a rigid sphere (1.5mm in diameter) in water. The simulation of the current work agrees well with the measurement ^[36]. There is a recirculation region or swirl behind the solid particle. This swirl is not observed in fluid flow around a free bubble (zero shear velocity), as shown in **Figure 8**. **Figure 8** shows the fluid flow pattern and trajectories of $100\mu\text{m}$ inclusions around a 5mm bubble in molten steel. The tracer particles (7020 kg/m^3 density) follow the stream lines and tend to touch the surface of the bubble at the top point (exactly half-way around the bubble), as shown in Fig.8a. Particles with density larger than that of the liquid, such as solid particles in water in mineral processing, tend to touch the bubble before the top point (Fig.8b), while denser particles, such as inclusions in the molten steel, tend to touch the bubble after the top point (Fig.8c). Stochastic fluctuation of the turbulence makes the inclusions very dispersed, so attachment may occur at a range of positions (Fig.8d)

The average turbulent energy in the bulk of the liquid has little effect on the local turbulent energy distribution around the bubble. As shown in **Figure 9**, Case a) has 4 orders of magnitude larger average turbulent energy than in the far field liquid Case b), but has slightly smaller local turbulent energy around the bubble. This is because Case a) has a lower bubble terminal velocity than Case b). However, the average turbulent energy has a great effect on the inclusion motion according to Eq.13-14.

During the motion of bubbles in molten steel, the fluid flow pattern around the bubble will change as inclusions become attached, as shown in **Figure 10**. A recirculation region behind the bubble is generated even for only five $50\mu\text{m}$ inclusions attached on the surface of the bubble. This recirculation does not exist behind a bubble that is free from attached inclusions. Thus, the fluid flow pattern around a bubble with attached solid inclusions is more like that around solid particles, such as shown in Fig. 7. **Figure 11** indicates that high turbulent energy levels exist around the inclusions attached on a bubble, and the turbulent energy in the wake of the bubble becomes smaller with more attached inclusions. The turbulence level around the bubble in turn affects inclusion attachment (Eq.13-14). Also, forces on the particles will push them around the

bubble surface towards the back of the bubble. With the current attachment model, these phenomena are not included, so further study is needed.

C. *Inclusion Attachment Probability to Bubbles*

The calculated collision times (Eq.2) and film drainage times (Eq.3) of inclusions onto bubbles are shown in **Figure 12** for various inclusions in molten steel. Fig.12a shows that for wetting inclusions (with small contact angle), the film rupture time is very large, but for nonwetting inclusions usually encountered in steelmaking (contact angle $>90^\circ$) the film rupture time is very short (60-67 μ s.) Fig.12b indicates that the collision time and film drainage time both increase with increasing inclusion size, but the film drainage time increases more steeply. For inclusions smaller than $\sim 10\mu$ m, the collision time is larger than the film drainage time, so is not an important attachment mechanism.

The calculated normal distances from the center of 100μ m inclusions to the surface of a 1mm bubble are shown in **Figure 13** as function of time during the approach of inclusions to this bubble. The time interval when the distance is less than inclusion radius (50μ m) is the interaction time between the inclusion and the bubble, which is also shown in Fig.13. Larger inclusions require greater interaction times to attach, on the order of mili second.

The calculated attachment probability of inclusions ($d_p=5, 10, 20, 35, 50, 70, 100\mu$ m) to bubbles (1, 2, 4, 6, 10mm) are shown in **Figure 14a**, based on trajectory calculations of inclusions without considering the stochastic effect. To compute attachment rates for a continuous size distribution of inclusions and bubbles, regression was performed on these probabilities. The results are shown in Table I. The regression equation obtained, Eq.(16), is included in Fig.14.

$$P = Ad_p^B \quad (16)$$

where A and B are

$$A = 0.268 - 0.0737d_B + 0.00615d_B^2 \quad (17)$$

$$B = 1.077d_B^{-0.334} \quad (18)$$

where d_B is in mm, d_p is in μ m.

Eq.(16) should be used under the following conditions: 1). Bubble size is in the range of 1-10mm, and 2) bulk turbulent energy level is less than $10^{-2} \text{ m}^2/\text{s}^2$. The attachment probability of inclusions to the surface of the bubble for processes with turbulent energy $> 10^{-2} \text{ m}^2/\text{s}^2$, such as argon stirred ladles, is investigated elsewhere.^[37] In a continuous casting mold, the bubble size is less than 5mm, and the turbulent energy is in the order of $10^{-3} \text{ m}^2/\text{s}^2$, hence Eq.(16) can be used.

Fig.14b indicates that the regression equation matches roughly the numerical simulations. Fig.14c shows the calculated attached attachment probability as function of bubble size and inclusion size, according to Eq.(16). If bubble size is less than 6mm, smaller bubbles and larger inclusions have larger attachment probabilities. Small 1mm bubbles can have inclusion attachment probabilities as high as 30%, while the inclusion attachment probability to $>5\text{mm}$ bubbles is less than 1%. However, the attachment probability increases with increasing bubble size when bubbles are larger than 7. This is due to the increased rate of capture to spheroidal bubbles.

Typical attachment probabilities of inclusions to a bubble surface including the stochastic effects of the turbulent flow are shown in **Table II**. The Stochastic effect simulated by the random walk method slightly increases the attachment probability of inclusions to the bubble surface. **Figure 15** shows that this effect allows $50\mu\text{m}$ inclusions starting 4 bubble diameter from the column axis to collide and attach to the 1mm bubble surface. The largest attachment opportunity is at $\sim 2\text{mm}$ diameter. On the other hand, without considering the stochastic effect, only and all of the $50\mu\text{m}$ inclusions within 0.34mm of the column axis attach to the bubbles. Owing to the extra computational effort required for the stochastic model, it was not performed for all sizes of bubbles and inclusions. The Stochastic attachment probability was estimated from these two cases to be $16.5/11.6=1.4$ times of the non-Stochastic attachment probability.

IV. FLUID FLOW AND BUBBLE MOTION IN THE CONTINUOUS CASTING STRAND

A, Model Formulation and Flow Pattern

Three dimensional single-phase steady turbulent fluid flow in the SEN and continuous casting strand was modeled by solving the continuity equation, Navier-Stokes equations, and standard equations for transport of turbulent energy and its dissipation rate.^[38, 39] The trajectories of bubbles are calculated by Eqs.10-13, which include the effect of chaotic turbulent motion

using the Random Walk Model. Inclusion trajectories calculated with this approach match reasonably well with those by Large Eddy Simulation.^[40] Bubbles escape at the top surface and the open bottom of the 2.55m long mold domain, and are reflected at other faces. Bubbles, which escape from the bottom, are considered to eventually become entrapped by the solidifying shell. This is a crude preliminary approximation of flow and bubble transport, which is being investigated further as part of this project^[41]. The entrapment of particles into the solidifying shell is very complex and is receiving well-deserved attention in recent work.^[42-44]

The SEN is with 80mm bore size, and down 15° output angle, and 65×80mm output size. The submergence depth of the SEN is 300mm, and the casting speed is 1.2 m/min, corresponding to a steel throughput of 3.0 tonne/min. Half width of the mold is simulated in the current study (0.65m half width×0.25m thickness). The calculated weighted average turbulent energy and its dissipation rate at the SEN output are 0.20 m²/s³ and 5.27 m²/s³ respectively. The argon flow rate injected into the molten steel through the upper nozzle and upper slide gate is 10-15 Nl/min. According to previous multiphase fluid flow simulation^[45], under this argon gas flow rate, the fluid flow pattern in the current mold is still a double roll flow pattern. Thus, the current simplification that ignores momentum transfer from the bubbles to the fluid can roughly represent the real multiphase fluid flow in this mold.

The velocity vector distribution on the center face of the half strand is shown in **Figure 16**, indicating a double roll flow pattern. The upper loop reaches the meniscus of the narrow face, and the second loop takes steel downwards into the liquid core and eventually flows back towards the meniscus in the strand center. The calculated volume-average turbulent energy and its dissipation rate in the CC strand is 1.65×10^{-3} m²/s² and 4.22×10^{-3} m²/s² respectively.

B. *Bubble Trajectory Results*

Typical bubble trajectories are shown in **Figure 17**. Smaller bubbles penetrate and circulate more deeply than the larger ones. According to Fig.5, the maximum bubble size is around 5mm. Bubbles larger than 1mm mainly move in the upper roll, and are quickly removed. 0.2mm bubbles can recirculate with paths as long as 6.65m and 71.5s before they escape from the top or become entrapped through the bottom, while 0.5mm bubbles move 3.34m and 21.62s, 1mm bubbles move 1.67m and 9.2s, and 5mm bubbles move 0.59m 0.59s. The mean path length (L_B)

and the residence time (t_B) of 5000 bubbles each size are shown in Figure 18, and the following regression equations are obtained:

$$L_B = 9.683 \exp\left(-\frac{1000d_B}{0.418}\right) + 0.595 \quad (19)$$

$$t_B = 195.6 \exp\left(-\frac{1000d_B}{0.149}\right) + 23.65 \exp\left(-\frac{1000d_B}{0.139}\right) + 2.409 \exp\left(-\frac{1000d_B}{8.959}\right) \quad (20)$$

where the path length L_B and bubble size d_B are in m, and the residence time t_B is in s. Combining the path length and the residence time, the apparent average bubble speed is $W_B = L_B/t_B$. The following regression equation is obtained:

$$W_B = 0.170(1000d_B)^{0.487} \quad (21)$$

Larger bubbles have larger average speed, which can be as high as 0.5 m/s for 10mm bubbles.

V. INCLUSION REMOVAL BY BUBBLES IN THE CONTINUOUS CASTING STRAND

A. Model Formulation

A model of inclusion removal by bubble flotation is developed for the molten steel-alumina inclusion-argon bubble system by evaluating a simple algebraic equation that incorporates the results of the previous sections. The following assumptions are used:

- Bubbles all have the same size, and the bubble size and the gas flow rate are chosen independently;
- Inclusions have a size distribution and are uniformly distributed in the molten steel, and they are too small to affect bubble motion or the flow pattern;
- Only the inclusions removed by bubble flotation are considered. The transport and collision of inclusions are ignored.
- Once stable attachment occurs between a bubble and an inclusion, there is no detachment and the inclusion is considered to be removed from the molten steel, owing to the high removal fraction of most bubbles.

The number of inclusions i , $N_{A,i}$, with diameter $d_{p,i}$ which attach to a single bubble (sequence number j) with a diameter of d_B , during its motion through the molten steel is

$$N_{A,i} = \left(\frac{\pi}{4} d_{B,j}^2 \right) L_{B,j} \cdot n_{p,i} \Big|_j \cdot \frac{P_i}{100} \quad (22)$$

where L_B is the path length of the bubble (m), given by Eq.(19), P is the attachment probability of the inclusion to the bubble (%), given by Eq.(16), $n_{p,i} \Big|_j$ is the number density of inclusions with diameter $d_{p,i}$ when bubble j is injected, which can be represented by the following recursion equation

$$n_{p,i} \Big|_j = n_{p,i} \Big|_{j-1} \times \frac{(100 - P_i)}{100} \times \frac{\left(\frac{\pi}{4} d_B^2 \right) L_B}{V_M} \quad (23)$$

In evaluating this equation, the inclusion number density distribution is updated after the calculation of each individual bubble, in order to account for the significant change in inclusion concentration caused by the simultaneous inclusion removal of many bubbles.

In Eq.(23), V_m is the volume of molten steel entering the strand (m^3) in time t_B (s) and is

$$V_M = \frac{V_C}{60} S \cdot t_{B,j} \quad (24)$$

where casting speed V_C is in m/min, S is the area of the slab section ($=0.25 \times 1.3 \text{m}^2$),

The number density of inclusions ($1/\text{m}^3$ steel) of size i removed by attachment to a single bubble is

$$n_{A,i} = \frac{N_{A,i}}{V_M} \quad (25)$$

Assuming that all inclusions are Al_2O_3 , the oxygen removed by this single bubble j (in ppm) then can be expressed by

$$\Delta O_j = \sum_i \left[n_{A,i} \left(\frac{\pi}{6} d_{p,i}^3 \right) \frac{\rho_p}{\rho_M} \cdot \frac{48}{102} \cdot 10^6 \right] \quad (26)$$

which can be rewritten by inserting Eqs.22-25 into 26 and rearranging as

$$\Delta O_j = 1.16 \times 10^5 \cdot \frac{1}{V_C S} \frac{d_{B,j}^2 L_{B,j}}{t_{B,j}} \frac{\rho_p}{\rho_M} \sum_i \left(n_{p,i} \Big|_j \cdot P_i \cdot d_{p,i}^3 \right) \quad (27)$$

Because it is assumed that all bubbles in the molten steel have the same size, the total number of bubbles with diameter d_B entering the molten steel during time t_B is

$$n_B = \frac{1}{2} \frac{Q_G \cdot \frac{T_M}{273}}{\frac{\pi}{6} d_B^3} t_B \quad (28)$$

where Q_G is the gas flow in NI/min, T_M is the steel temperature (1823K), and the factor of $\frac{1}{2}$ is due to the simulation domain of a half mold.

The total oxygen removal by all of the bubbles can be expressed by

$$\Delta O = \sum_{j=1}^{n_B} \Delta O_j \quad (29)$$

B. *Results and Discussion*

The inclusion size distributions measured in the tundish above the outlets and in the CC slab are shown in **Figure 19a** together with the calculated size distributions after inclusion removal by bubble flotation for several different bubble sizes. The corresponding inclusion removal fractions are shown in Fig.19 b). If the bubbles are larger than 5mm, less than 10% of the inclusions can be removed by bubble flotation at the gas flow rate of 15 NI/min. This corresponds to a 3ppm decrease in total oxygen, as shown in **Figure 20**. Smaller bubbles appear to enable more inclusion removal for the same gas flow rate. Specifically, 1mm bubbles remove almost all of the inclusions larger than 30 μ m. However, it is unlikely that all of the bubbles that are this small could escape from the top surface. Those that are entrapped in the solidifying shell would generate serious defects in the steel product, such as shown in Fig.1-2. Increasing bubble size above ~7mm produces less change in removal rate, due to the change in bubble shape offsetting the smaller number of bubbles.

Increasing gas flow rate naturally causes more inclusion removal by bubble flotation, as shown in Fig.20. Considering the effect of turbulent stochastic motion slightly increases inclusion removal by bubble flotation. For the current CC conditions, including a gas flow rate of 15 NI/min, the bubble size is likely to be around 5mm, assuming there are a large number of active sites on the porous refractory that cause a gas flow rate of <0.5 ml/pore. ^[46] As shown in Fig. 20, about 10% total oxygen is removed by bubble flotation. Previous investigations indicate

that ~8% of the inclusions are removed to the top surface due to flow transport in the CC mold region. [47] Thus, the total predicted inclusion removal by flow transport and by bubble flotation is around 18%. The measured inclusion mass fraction is 66.8ppm in the tundish, and averages 51.9ppm in the slab, which corresponds to 22% removal in the mold (Fig.19). The prediction and the measurement agree remarkably well, considering that some inclusions are likely entrapped to the SEN walls to cause clogging and others float to the slag layer without the aid of bubbles.

Decreasing bubble size is shown in Figs. 19 and 20 to be more efficient at removing inclusions. As already mentioned before, however, small bubbles, such as those $< 1\text{mm}$, may be trapped into solidifying shell while moving through the lower recirculation zone. Thus, there should be an optimum bubble size, which gives not only high inclusion removal efficiencies, but also low entrapment rates. The present results suggest the optimal size might be from 2-4mm.

Due to capturing many inclusions on its surface, the apparent density of a bubble with attached inclusions increases. According to the current fluid flow and inclusions condition in the CC mold, the calculated apparent density of the bubble decreases with increasing bubble size (**Figure21a**). The maximum apparent bubble density is only around 5.0kg/m^3 . Although this is much greater than the original argon gas density of 1.6228 kg/m^3 , it is still far smaller than that of the molten steel, so has little effect on the bubble motion or bubble residence time in the strand (Eq.(11)). The inclusions attached to each bubble also have a size distribution, as shown in Fig.21b. There are typically several thousand inclusions predicted to be attached to the bubble surface, which matches well with the measurements in Fig.21c. Larger bubbles capture more inclusions than smaller ones (Fig.21b) per bubble. This is insufficient to make up for their smaller number, and furthermore makes them more dangerous if captured. Thus large bubbles should be avoided.

VI. SUMMARY AND CONCLUSIONS

This work presents a fundamental approach to modeling inclusion removal due to bubble flotation in molten steel processing. The problem of multiple length and time scales is addressed by dividing the modeling into two modeling stages: 1) fundamentals of inclusion-bubble interactions that are independent of the macro-scale process, and 2) macro scale flow phenomena that can incorporate the results of the micro-scale effects. The small-scale model is validated

with available measurements and applied to predict the changes in inclusion distribution that occur in the mold region of a continuous slab caster. Specific model findings include:

- 1) In molten steel, bubbles smaller than 3mm tend to spherical, 3-10mm bubbles are spheroidal, and bubbles larger than 10mm are spherical –cap shaped. The bubble size depends mainly on the gas flow rate, injection method and stirring power in the molten steel. The average equivalent size of bubbles is estimated to be ~5mm in the CC mold investigated in this work.
- 2) Inclusions tend to pass the midpoint of the bubble and first touch the bubble surface towards the bottom side, although stochastic fluctuations due to turbulence cause many variations. The fluid flow pattern around a bubble with attached solid inclusions is similar to that of flow around a large solid particle. Inclusions attached to the bubble surface also increase the turbulent kinetic energy distributed around the bubble.
- 3) Smaller bubbles and larger inclusions have larger attachment probabilities. Bubbles smaller than 1mm diameter have inclusion attachment probabilities as high as 30%, while the inclusion attachment probability for bubbles larger than 5mm is less than 1%. The stochastic effect of turbulence (modeled by the random walk method) slightly increases the attachment rate.
- 4) In the continuous casting strand, smaller bubbles penetrate and circulate more deeply than larger ones. Bubbles larger than 1mm mainly move in the upper roll moving 0.6-1.7m in 0.6-9.2s. Smaller bubbles can move over 6m and take over 60s before they either escape from the top surface or are entrapped through the bottom.
- 5) In the continuous casting mold, if the bubbles are ~ 5mm in diameter, ~10% of the inclusions are predicted to be removed by bubble flotation, corresponding to around 3ppm decrease in total oxygen. Combined with ~ 8% inclusion removal by flow transport, the total is comparable with the measured inclusion removal rate by the CC mold of ~22%.
- 6) Smaller bubbles are more efficient at inclusion removal by bubble flotation, so long as they are not entrapped in the solidifying shell. Larger gas flow rate favors inclusion removal by bubble flotation. The optimum bubble size might be 2-4mm.

- 7) Attached inclusions increase the bubble density by several times, but do not affect its motion because the apparent density is still far smaller than that of molten steel.

Future research using this methodology is needed to investigate:

- The stochastic probability of all inclusion and bubble sizes,
- The effect of bubble size distribution,
- Multiphase fluid flow including momentum exchange between phases,
- The effect of inclusion collisions,
- The entrapment of bubbles and inclusions into the solidifying steel shell
- Other process such as inclusion removal by bubble flotation in gas stirred ladles.

ACKNOWLEDGMENTS

This material is based upon work supported by the U.S. Department of Energy under cooperative agreement number DE-FC36-03ID14279. Such support does not constitute an endorsement by DOE of the views expressed in the article. This research is also supported by the National Science Foundation (Grant DMI-0115486) and the Continuous Casting Consortium at UIUC.

Captions:

Table I.	Regressed inclusion attachment probability to the bubble larger than 1mm.
Table II	Attachment probabilities of inclusions with and without random walk to a 1mm bubble
Fig.1	Inclusions outlining the former surface of bubbles captured in ingot steel (a,b,c) and in continuous cast steel (d)
Fig.2	Inclusion sliver in longitudinal section of a rolled sheet product (a), and pencil pipe lamination defect on a steel sheet (b).
Fig.3	Schematic of the attachment probability of inclusions to the bubble surface
Fig.4	Bubble shape characterized by its aspect ratio (e) as a function of its size
Fig.5	Maximum argon bubble size in turbulent molten steel with bulk stirring powers of different vessels
Fig.6	Bubble terminal rising velocity variation with stirring power (analytical models 1-5 refer to zhang's study)
Fig.7	Fluid flow behind a rigid sphere (1.5mm in diameter) in water: (a): experiment ^[36] ; (b): streamline by simulation; (c) velocity by simulation
Fig.8	Fluid flow and trajectories of 100 μ m inclusions around a 5mm bubble in the molten steel with density of 7020 kg/m ³ (a) Neutral-buoyancy particles (7020 kg/m ³); (b) denser particles (14040 kg/m ³); (c) Inclusions (2800 kg/m ³); (d) random walk of inclusions)
Fig.9	Turbulent energy distribution (1000k, in m ² /s ²) around a 1mm bubble (a: bulk turbulent energy 1.62×10^{-4} m ² /s ² , and its dissipation rate 1.43×10^{-3} m ² /s ³ , 1.292 m/s bubble terminal velocity; b: bulk turbulent energy 1.06×10^{-8} m ² /s ² , and its dissipation rate 2.74×10^{-7} m ² /s ³ , and 1.620 m/s bubble terminal velocity)
Fig.10	Fluid flow pattern around a 1mm bubble with (a) zero, (b) 5, (c) 12 and (d) 53 50 μ m inclusions attached
Fig.11	Turbulent energy distribution (1000k in m ² /s ²) around a 1mm bubble with (a) zero, (b) 5, (c) 12 and (d) 53 50 μ m inclusions attached
Fig.12	The collision time and film drainage time of inclusions onto different size bubbles
Fig.13	Computed normal distance from the center of 100 μ m inclusions to the surface of a 1mm bubble (a), and interaction times (b)
Fig.14	Calculated attachment probability of inclusions to bubbles
Fig.15	Attachment probability of 50 μ m inclusions to a 1mm bubble including stochastic effect of turbulence

- Fig.16 Flow pattern in the CC strand center face with half width (a: velocity vectors; b: streamline; c: turbulent energy dissipation rate $1000\epsilon \text{ m}^2/\text{s}^3$ and d: turbulent energy $100k \text{ m}^2/\text{s}^2$ respectively)
- Fig.17 Typical bubble trajectories in the mold with half width
- Fig.18 The mean path lengths, residence times and apparent speed of bubbles in the CC strand
- Fig. 19 Measured and calculated inclusion size distribution with different size bubble flotation (15 Nl/min gas)
- Fig. 20 Calculated inclusion removal by bubble flotation
- Fig.21 The calculated apparent density of bubbles with attached inclusions (a) and the calculated (b) and measured (c) number of inclusions attached on the bubble in the steel

Table I. Regressed inclusion attachment probability to the bubble larger than 1mm.

Bubble diameter	Attachment probability (%)
1mm	$P = 0.189d_p^{1.082}$
2mm	$P = 0.125d_p^{0.817}$
4mm	$P = 0.0570d_p^{0.722}$
5mm	$P = 0.0523d_p^{0.634}$
10mm	$P = 0.130d_p^{0.444}$

Table II Attachment probabilities of inclusions with and without random walk to a 1mm bubble

		Case 1	Case 2	
Average turbulent energy (m^2/s^2)		1.62×10^{-4}	1.06×10^{-8}	
Average turbulent energy dissipation rate (m^2/s^2)		1.43×10^{-3}	2.74×10^{-7}	
Bubble velocity (m/s)		1.292	1.620	
Bubble diameter (mm)		1	1	
Inclusions diameter (μm)		50	50	100
Attachment probability(%)	Non-Stochastic model	11.6	13.1	27.8
	Stochastic model	16.5	/	29.4

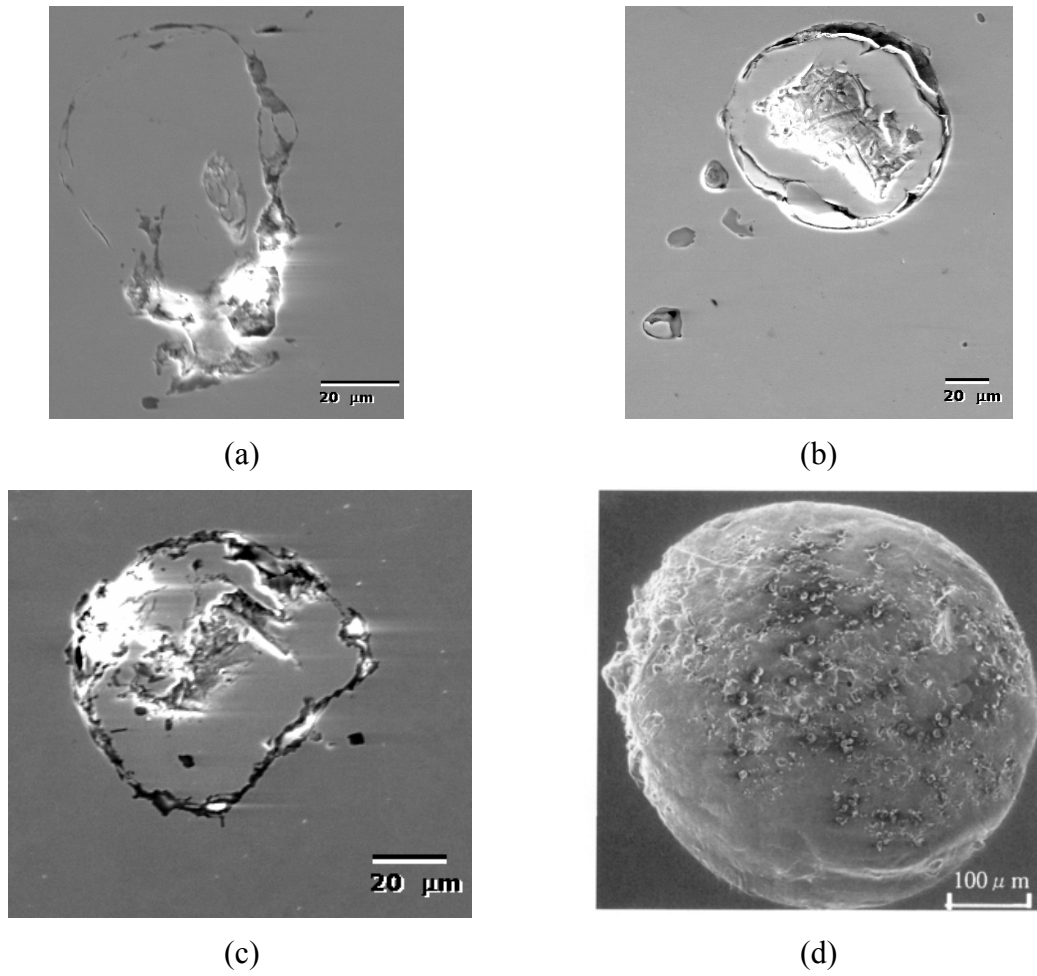
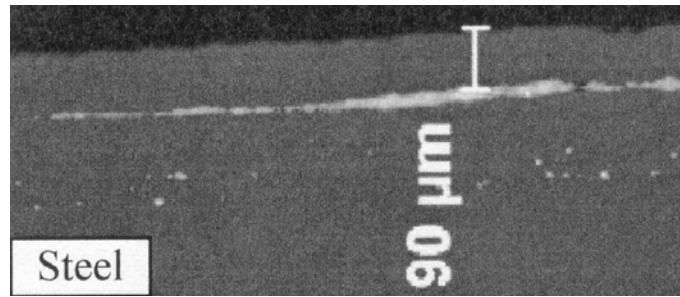
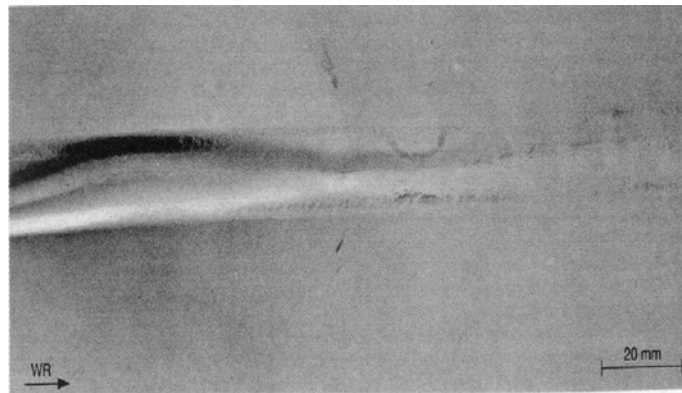


Fig.1 Inclusions outlining the former surface of bubbles captured in ingot steel (a,b,c)^[13] and in continuous cast steel (d^[14])



(a)



(b)

Fig.2 Inclusion sliver in longitudinal section of a rolled sheet product (a) ^[17], and pencil pipe lamination defect on a steel sheet (b) ^[15].

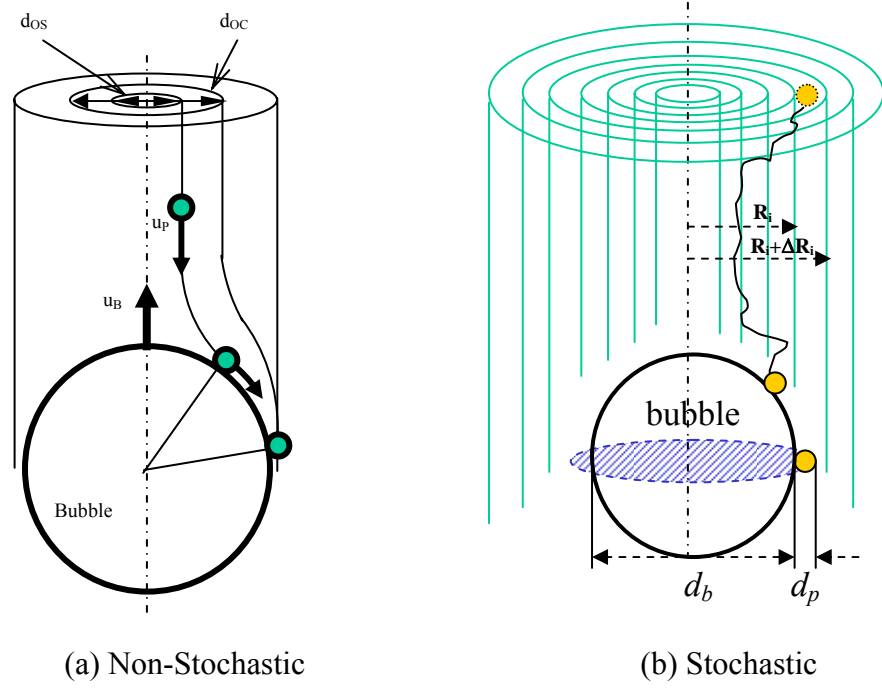


Fig.3 Schematic of the attachment probability of inclusions to the bubble surface

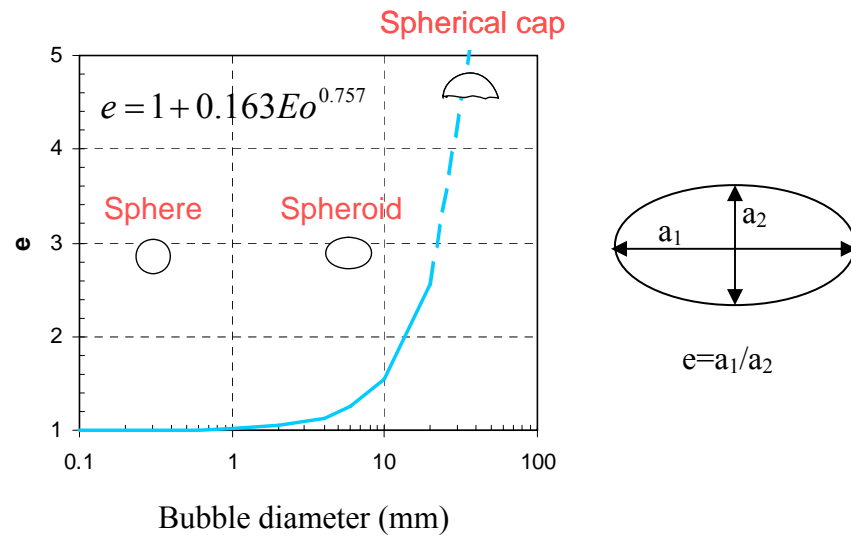


Fig.4 Bubble shape characterized by its aspect ratio (e) as a function of its size ^[25]

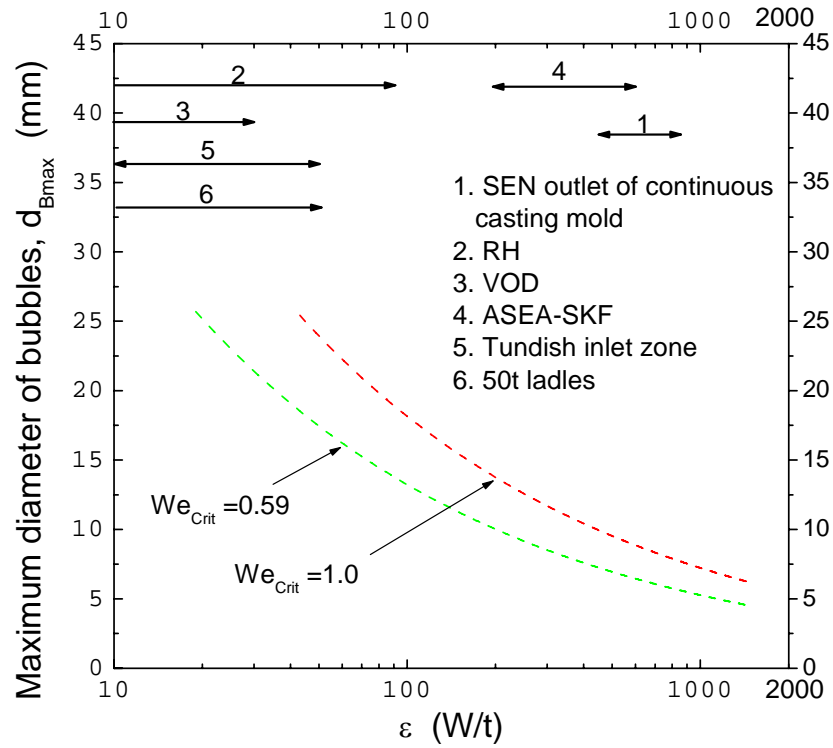


Fig.5 Maximum argon bubble size in turbulent molten steel with bulk stirring powers of different vessels ^[3]

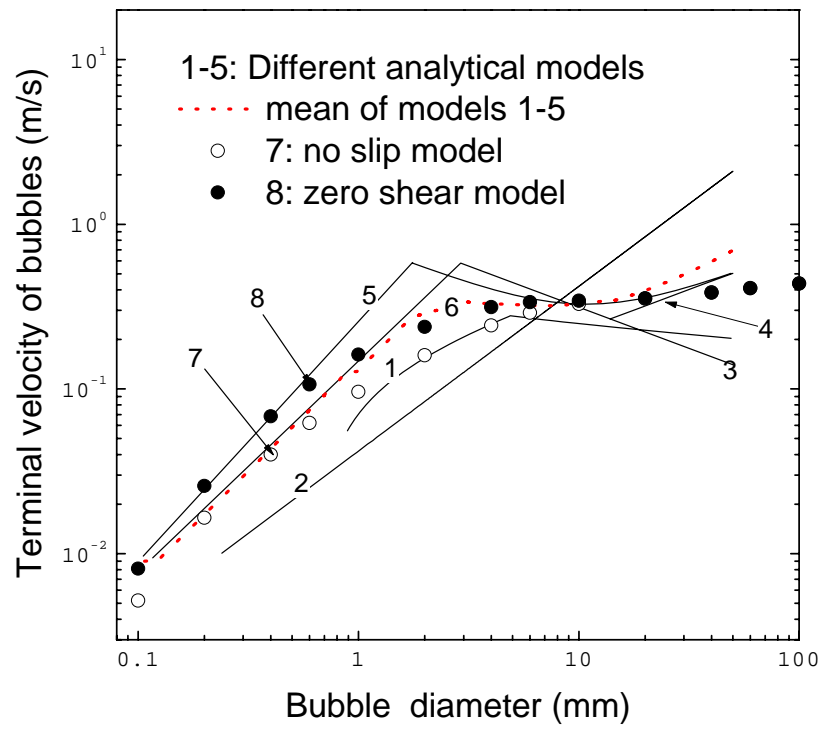


Fig.6 Bubble terminal rising velocity variation with stirring power (analytical models 1-5 refer to zhang's study ^[3])

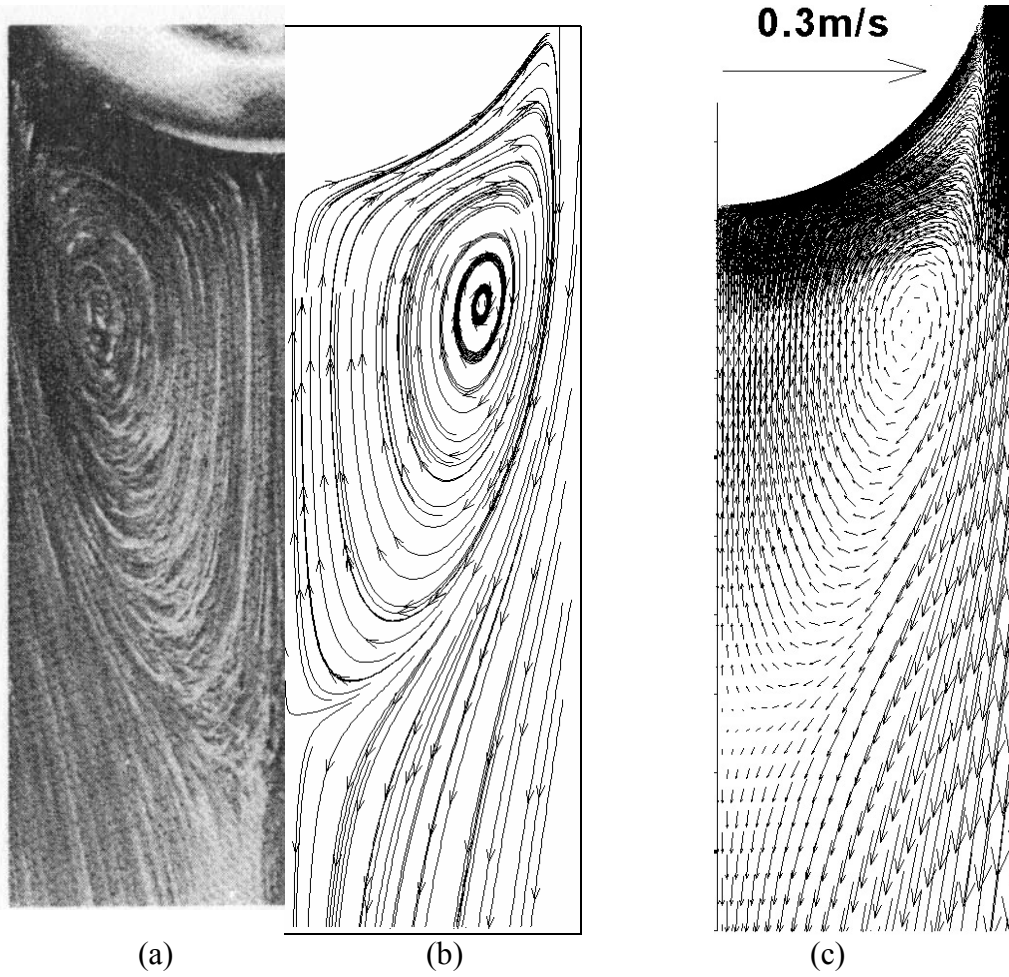


Fig.7 Fluid flow behind a rigid sphere (1.5mm in diameter) in water: (a): experiment ^[36]; (b): streamline by simulation; (c) velocity by simulation

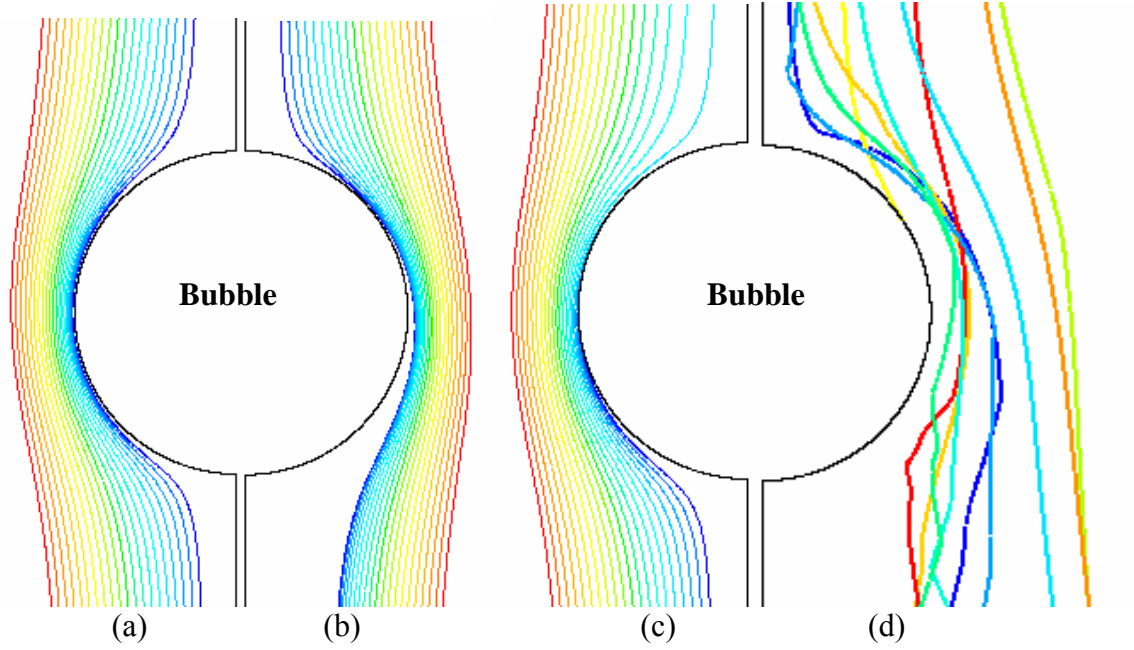
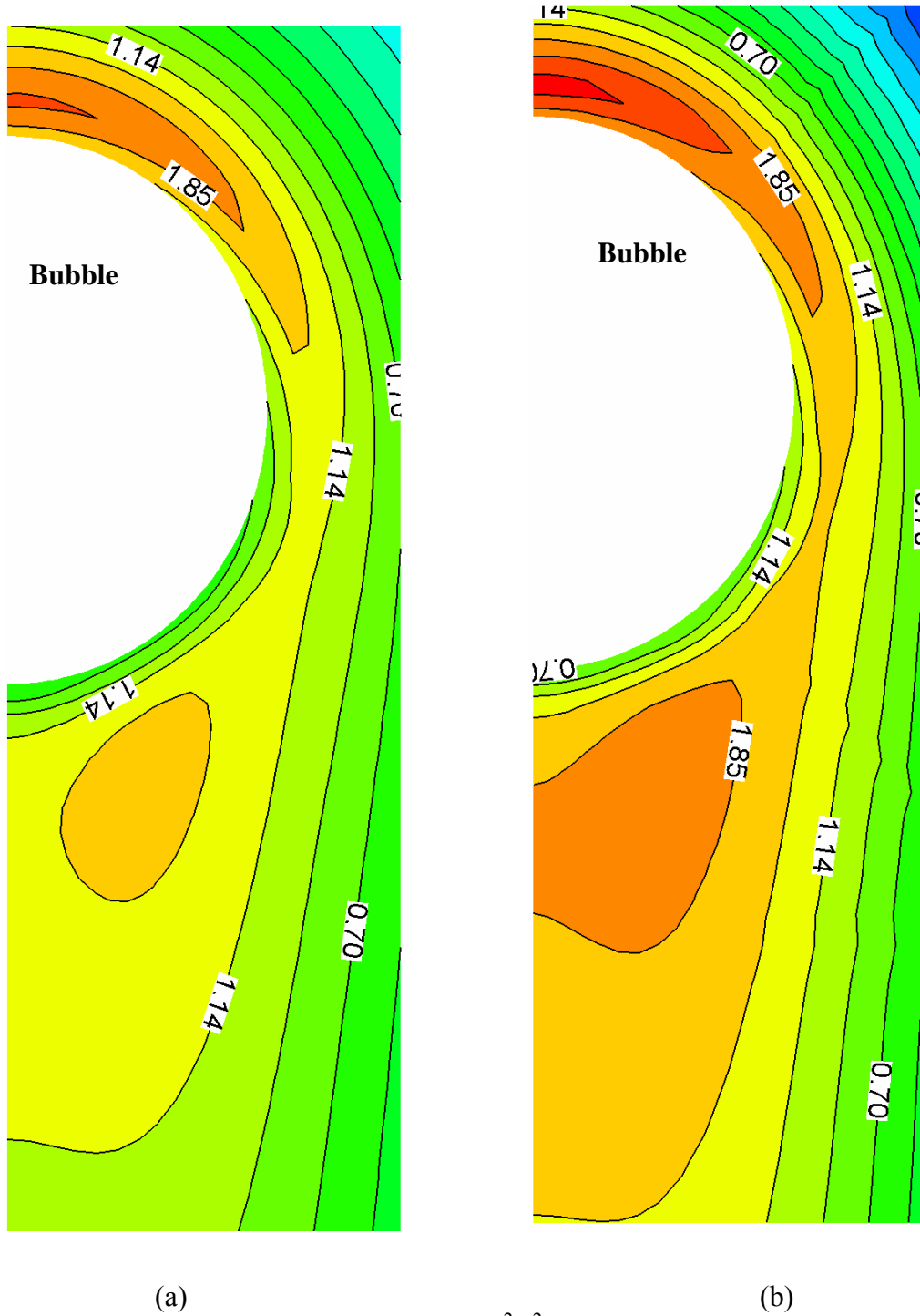


Fig.8 Fluid flow and trajectories of 100μm inclusions around a 5mm bubble in the molten steel with density of 7020 kg/m³ (a) Neutral-buoyancy particles (7020 kg/m³); (b) denser particles (14040 kg/m³); (c) Inclusions (2800 kg/m³); (d) random walk of inclusions)



(a) (b)

Fig.9 Turbulent energy distribution ($1000k$, in m^2/s^2) around a 1mm bubble (a: bulk turbulent energy $1.62 \times 10^{-4} \text{ m}^2/\text{s}^2$, and its dissipation rate $1.43 \times 10^{-3} \text{ m}^2/\text{s}^3$, 1.292 m/s bubble terminal velocity; b: bulk turbulent energy $1.06 \times 10^{-8} \text{ m}^2/\text{s}^2$, and its dissipation rate $2.74 \times 10^{-7} \text{ m}^2/\text{s}^3$, and 1.620 m/s bubble terminal velocity)

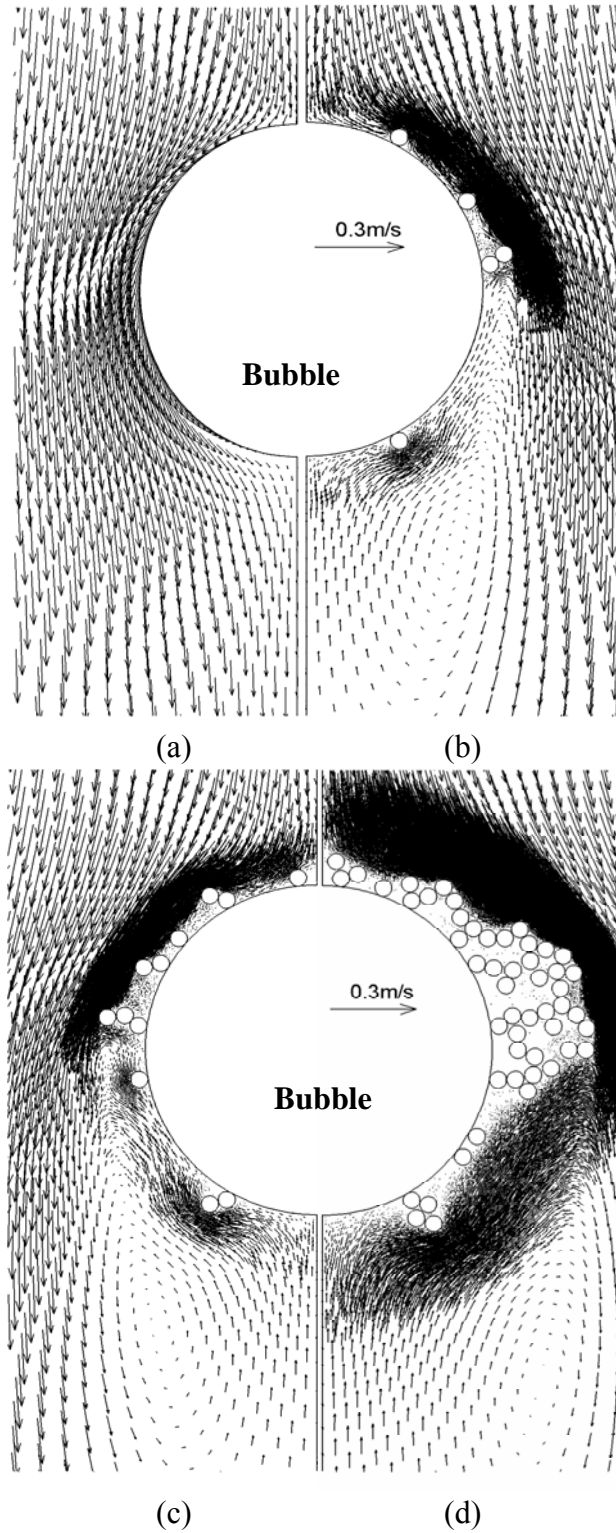


Fig.10 Fluid flow pattern around a 1mm bubble with (a) zero, (b) 5, (c) 12 and (d) 53 50 μ m inclusions attached

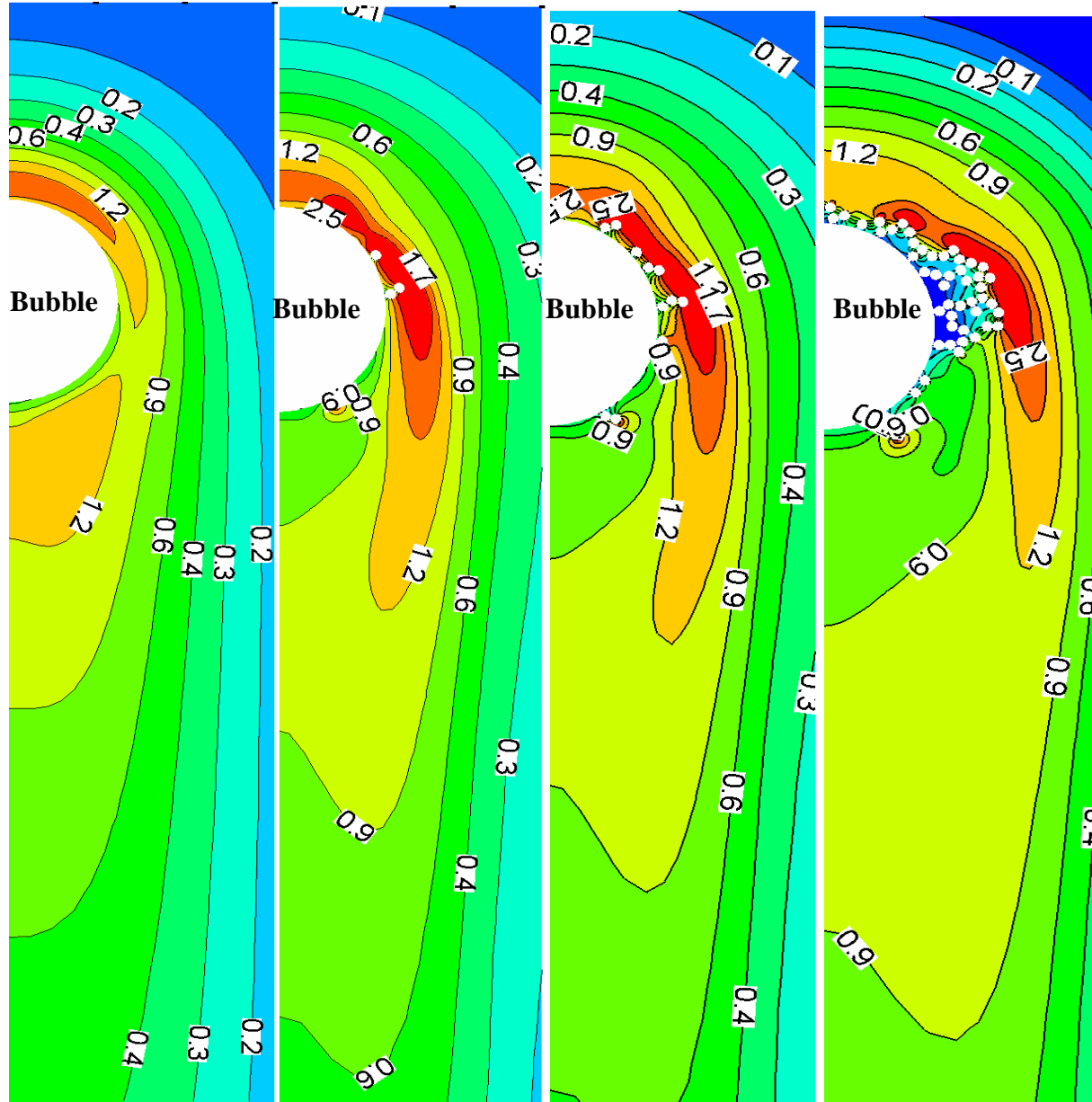
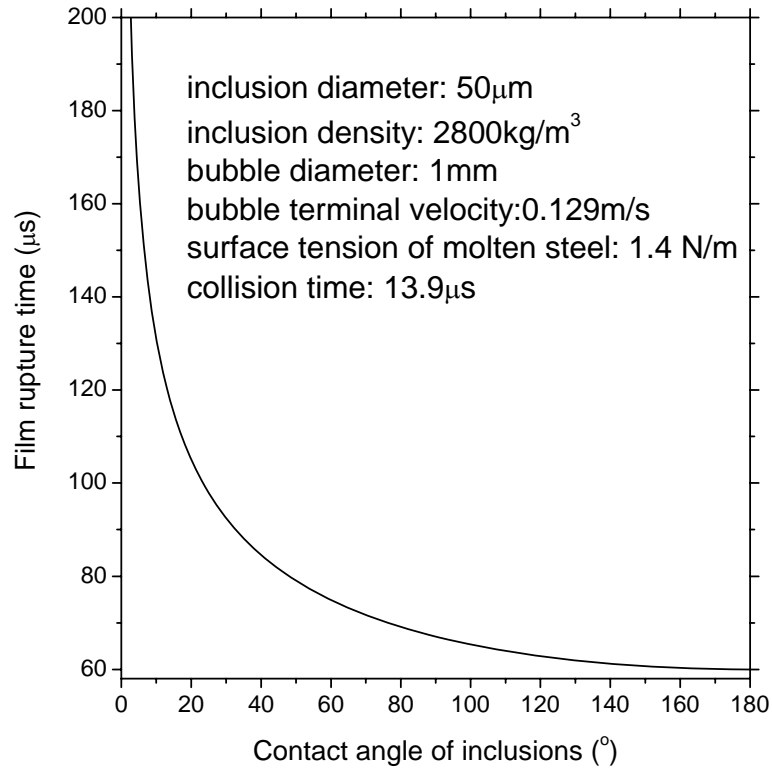
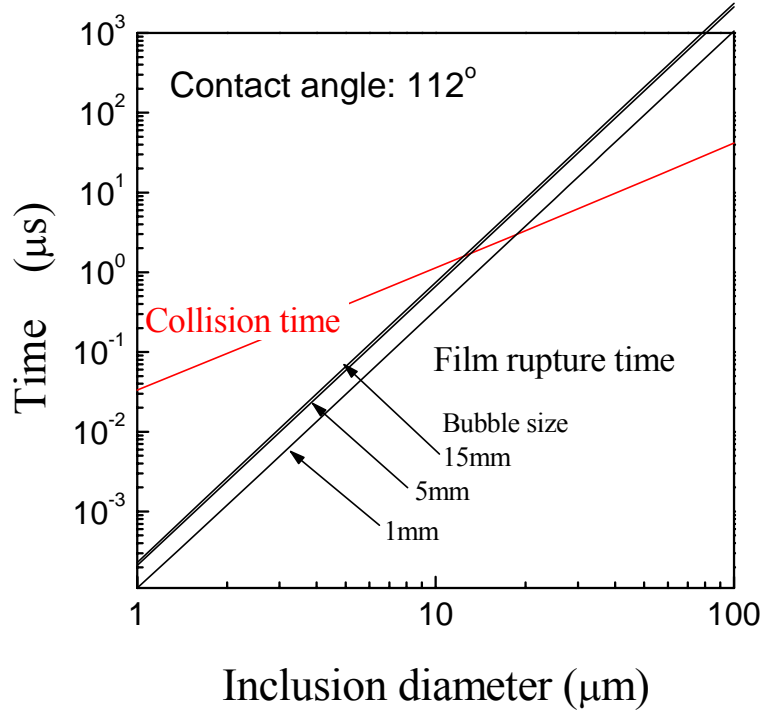


Fig.11 Turbulent energy distribution ($1000k$ in m^2/s^2) around a 1mm bubble with (a) zero, (b) 5, (c) 12 and (d) 53 $50\mu\text{m}$ inclusions attached

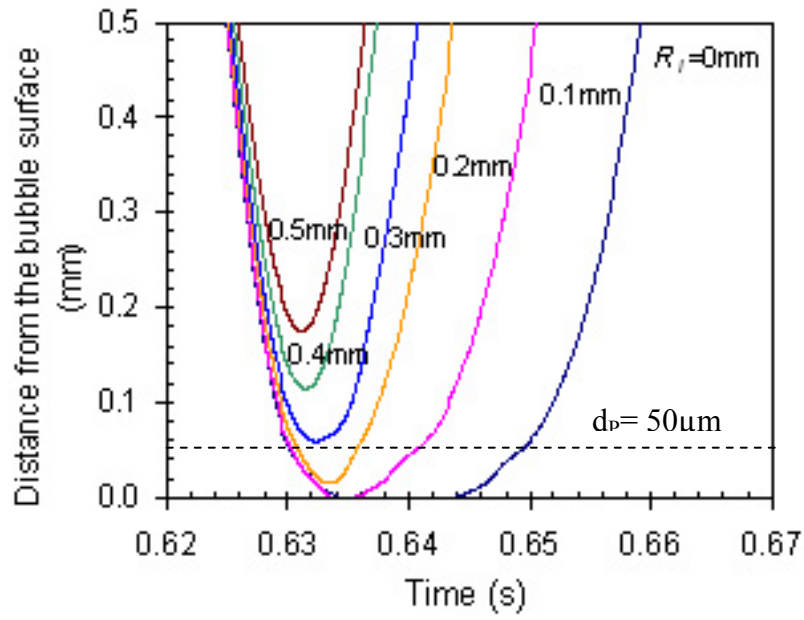


(a)

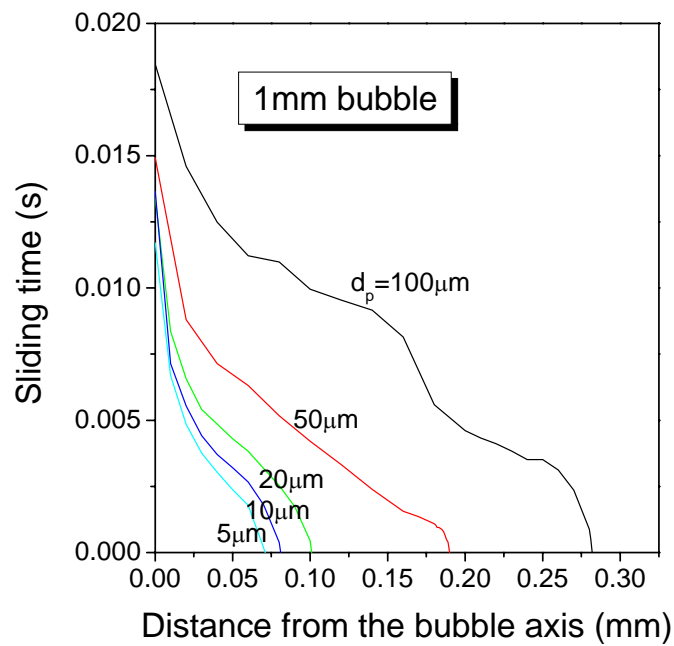


(b)

Fig.12 The collision time and film drainage time of inclusions onto different size bubbles

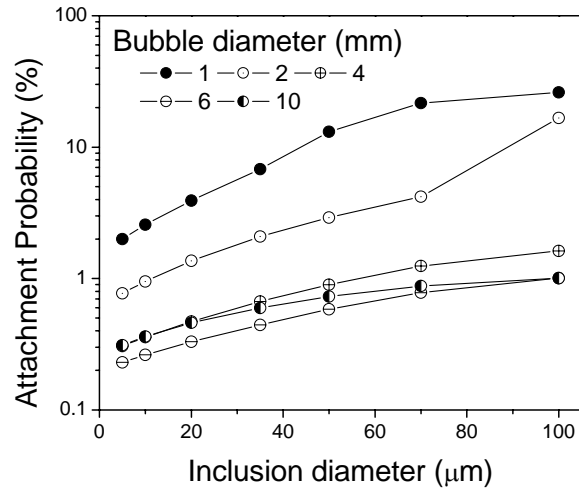


(a)

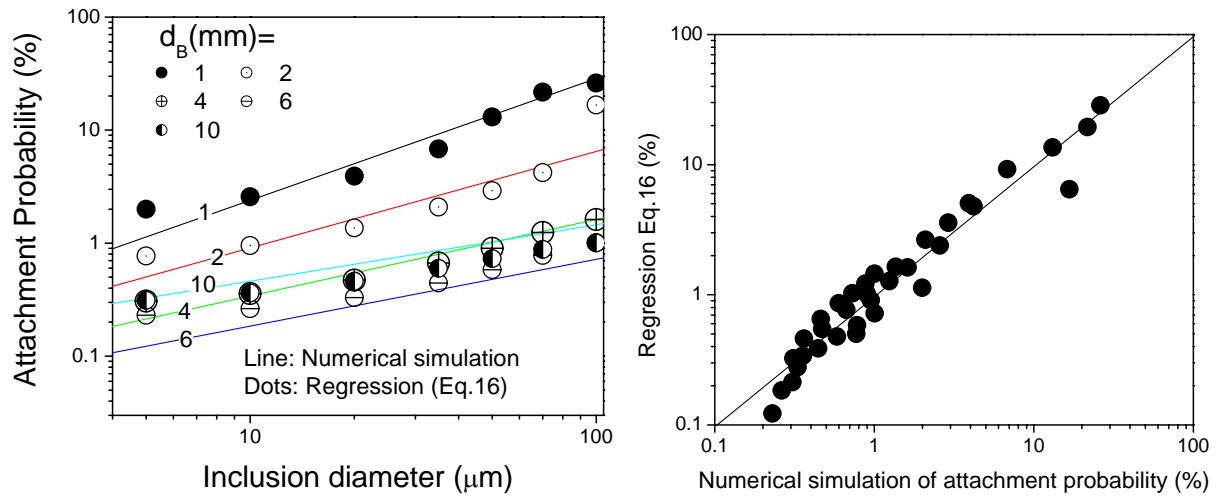


(b)

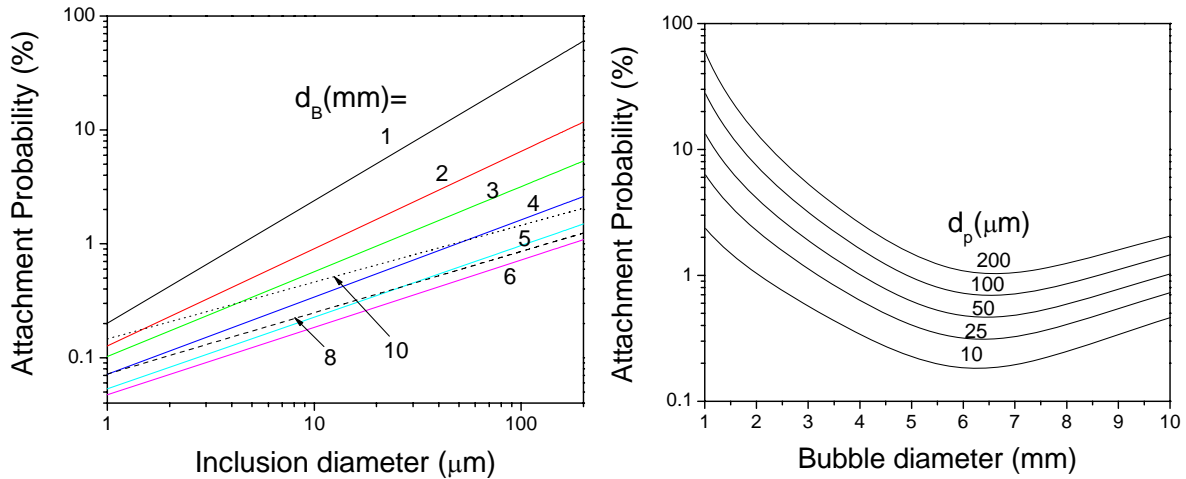
Fig.13 Computed normal distance from the center of 100μm inclusions to the surface of a 1mm bubble (a), and interaction times (b)



(a) Numerical simulation (NS)



(b) Comparison of numerical simulation and regression Eq. 16



(c) Attachment probability as function of inclusion size and bubble size (regression Eq. 16)

Fig. 14 Calculated attachment probability of inclusions to bubbles

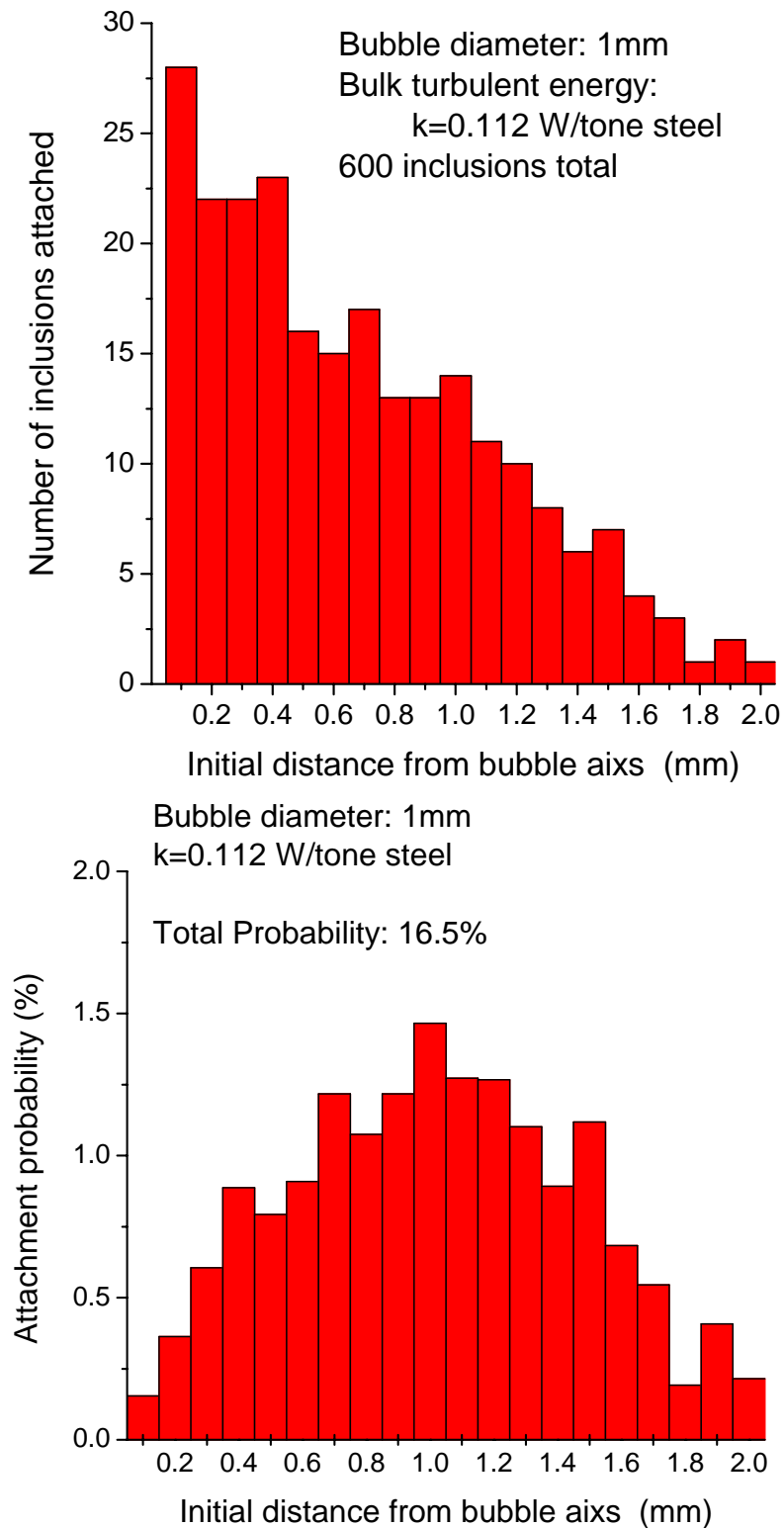


Fig.15 Attachment probability of 50 μ m inclusions to a 1mm bubble including stochastic effect of turbulence

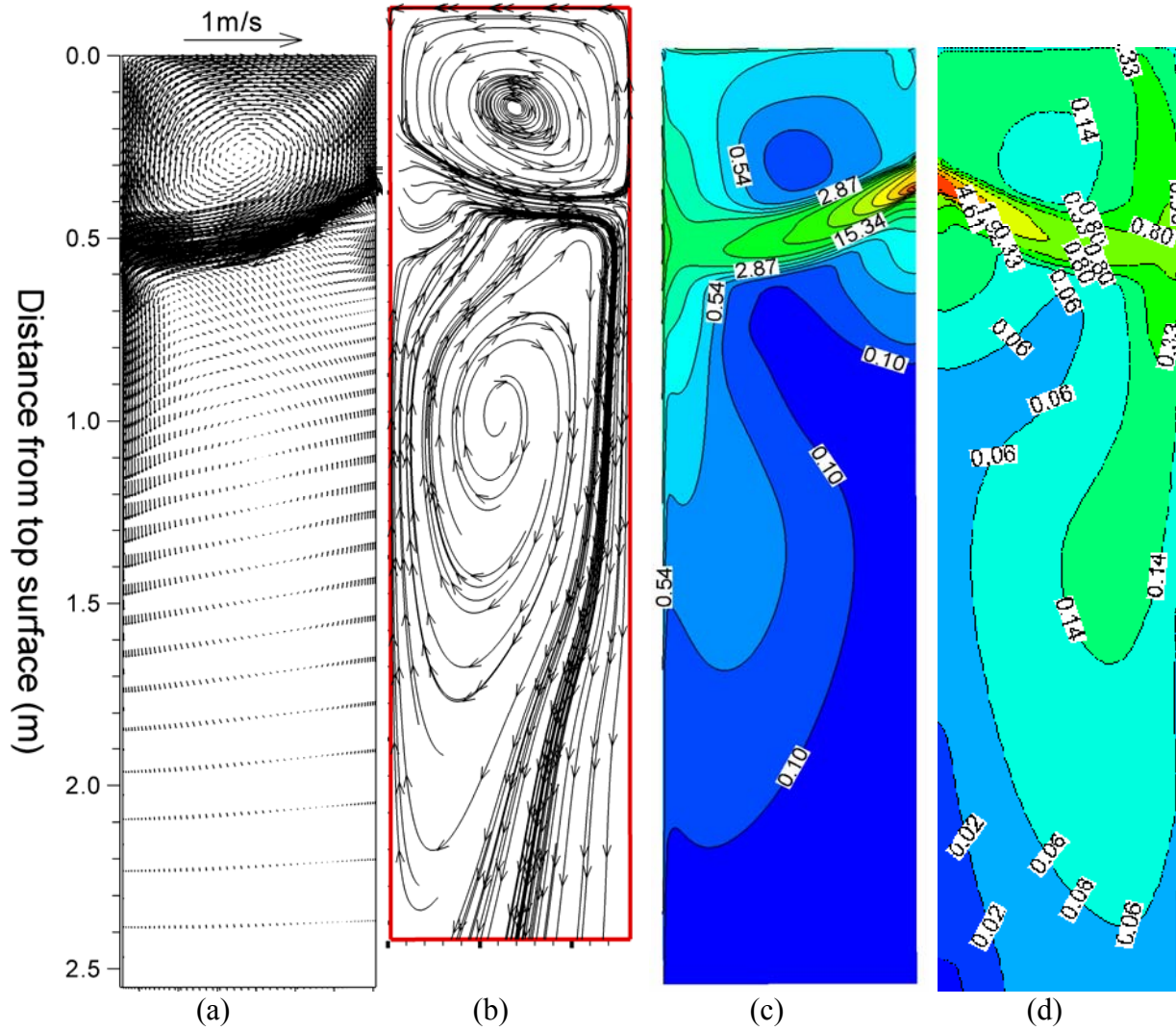


Fig.16 Flow pattern in the CC strand center face with half width (a: velocity vectors; b: streamline; c: turbulent energy dissipation rate $1000\epsilon \text{ m}^2/\text{s}^3$ and d: turbulent energy $100\text{k m}^2/\text{s}^2$ respectively)

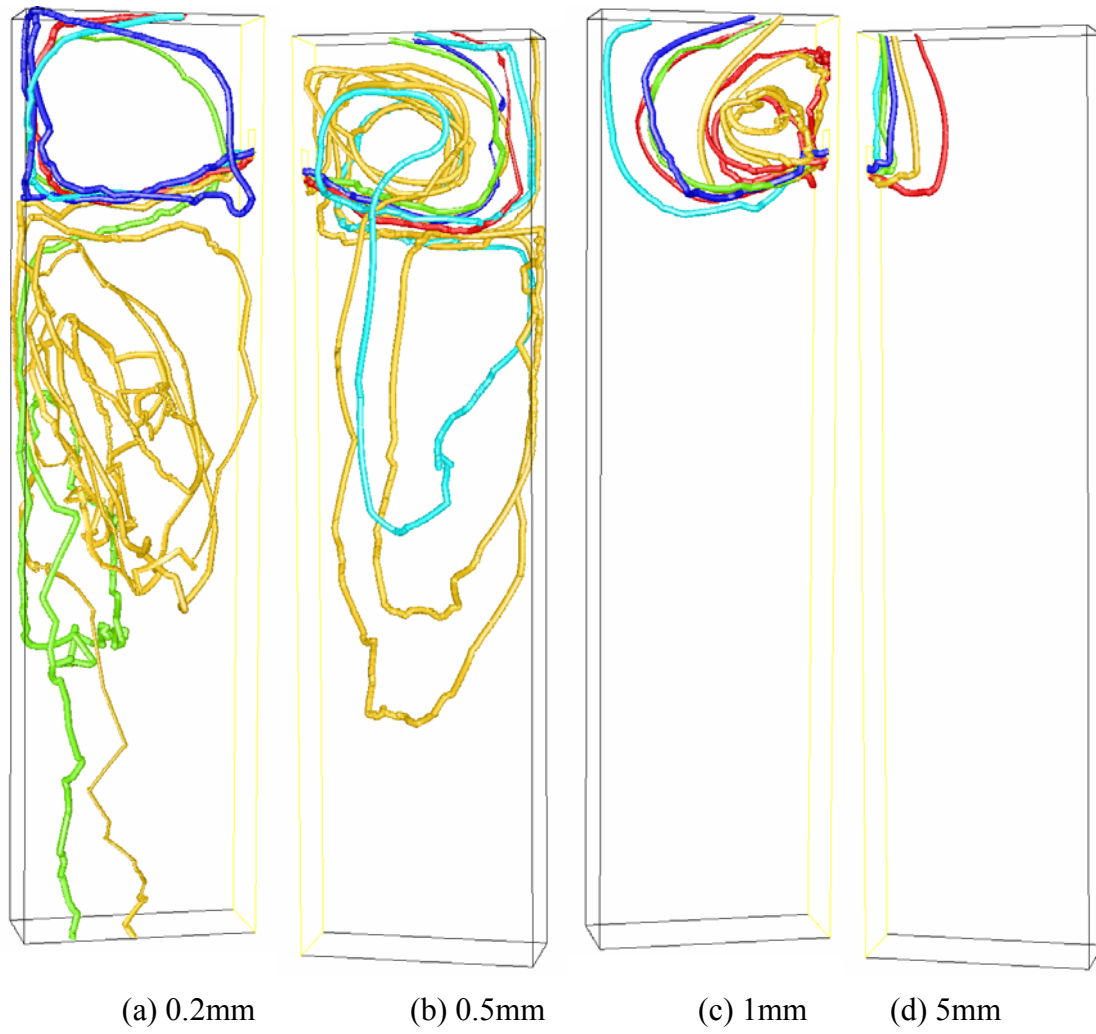


Fig.17 Typical bubble trajectories in the mold with half width

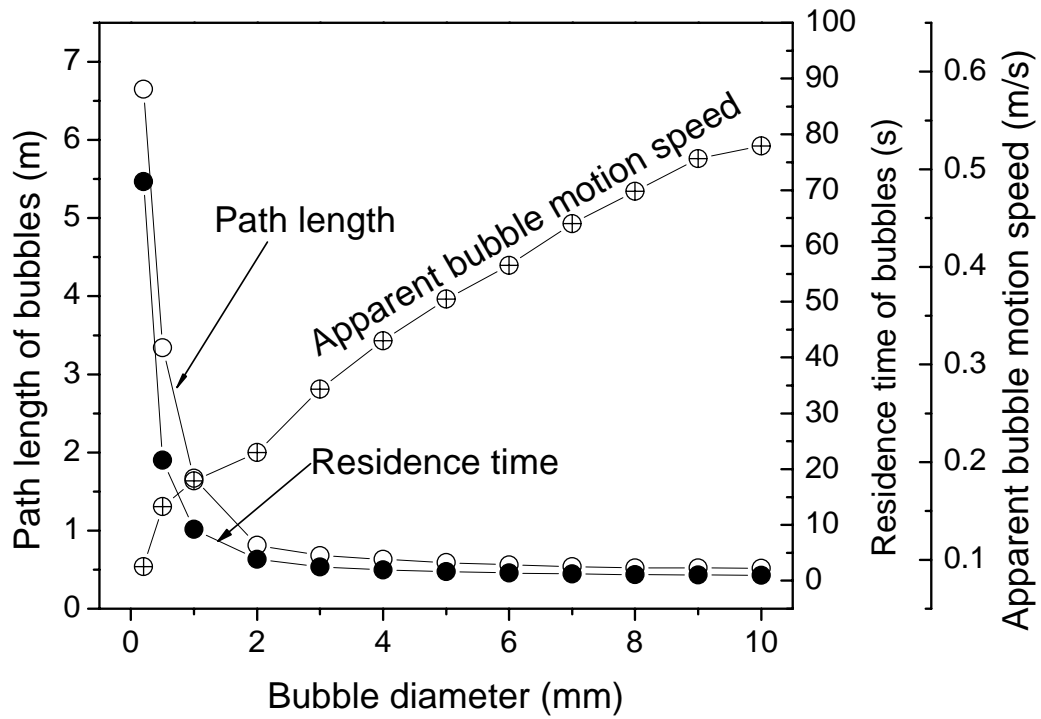
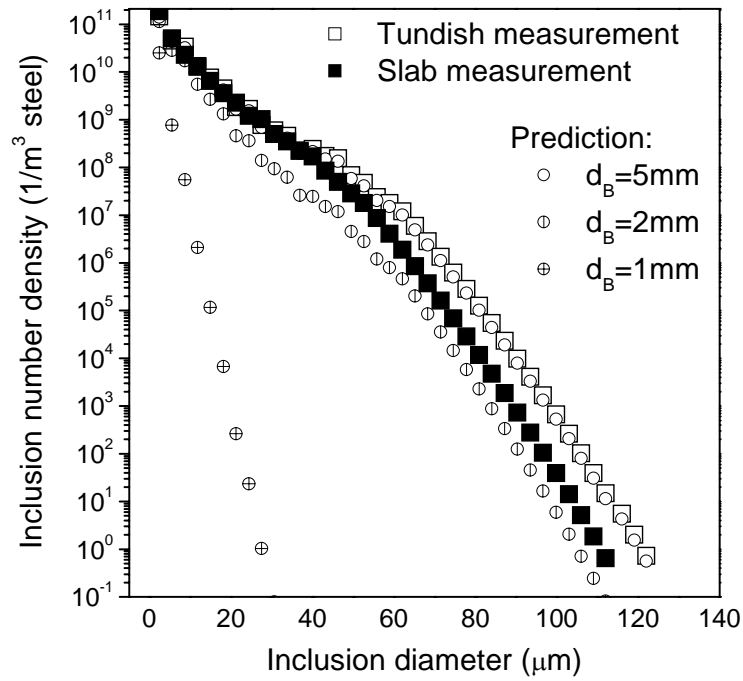
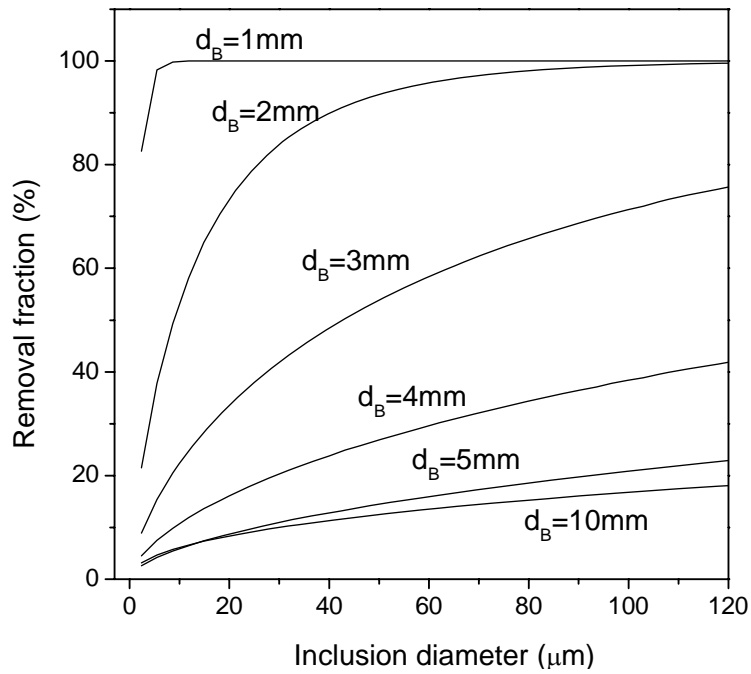


Fig.18 The mean path lengths, residence times and apparent speed of bubbles in the CC strand



(a)



(b)

Fig. 19 Measured and calculated inclusion size distribution with different size bubble flotation (15 Nl/min gas)

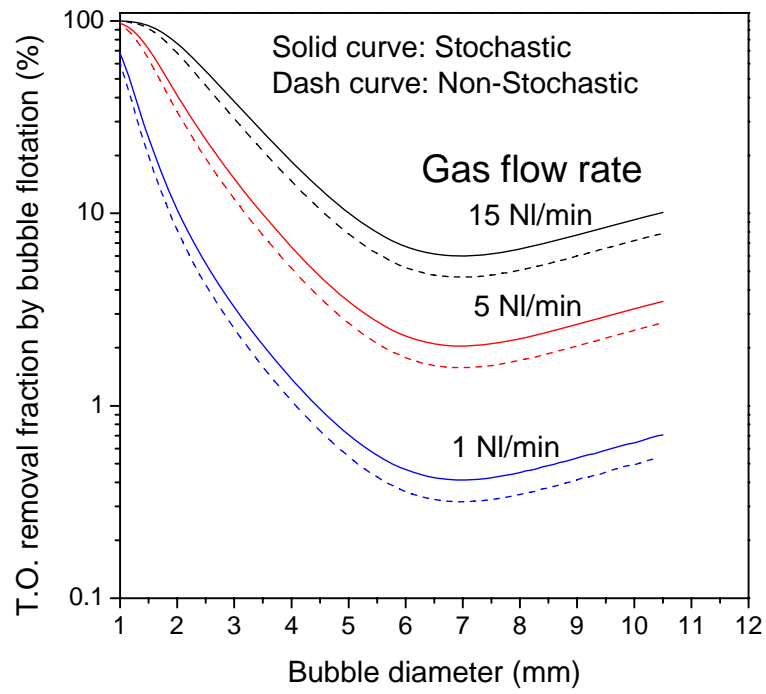


Fig. 20 Calculated inclusion removal by bubble flotation

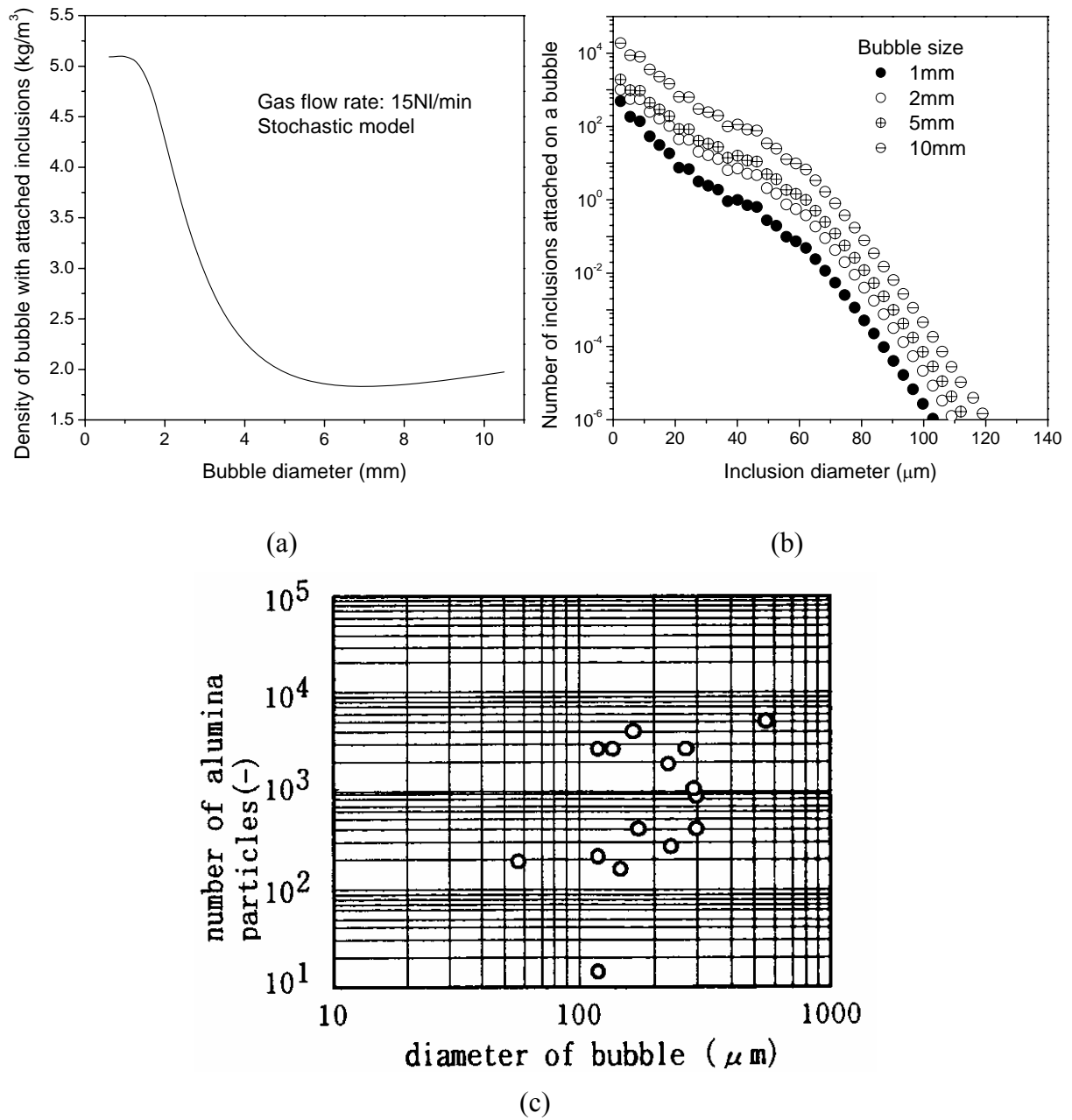


Fig.21 The calculated apparent density of bubbles with attached inclusions (a) and the calculated (b) and measured (c^[9]) number of inclusions attached on the bubble in the steel

References

- [1]. W. Pan, K. Uemura and S. Koyama, "Cold Model Experiment on Entrapment of Inclusions in Steel by Inert Gas Bubbles," *Tetsu-to-Hagane*, Vol. 78 (8), 1992, 87-94.
- [2]. L. Wang, H.-G. Lee and P. Hayes, "Modeling of air ingress and pressure distribution in ladle shroud system for continuous casting of steel," *Steel Res.*, Vol. 66 (7), 1995, 279-286.
- [3]. L. Zhang and S. Taniguchi, "Fundamentals of Inclusions Removal from Liquid Steel by Bubbles Flotation," *International Materials Reviews*, Vol. 45 (2), 2000, 59-82.
- [4]. L. Zhang, "Mathematical Simulation of Fluid Flow in Gas-Stirred Liquid Systems," *Modelling Simul. Mater. Sci. Eng.*, Vol. 8 (4), 2000, 463-476.
- [5]. L. Zhang and S. Taniguchi, "Fluid Flow and Particle Removal by Bubble Flotation in a Mechanically Stirred Vessel," *Materials Processing in the Computer Age III*, 2000, 111-122.
- [6]. L. Zhang and S. Taniguchi, "Water Model Study on Inclusion Removal by Bubble Flotation from Liquid Steel by Bubble Flotation under Turbulent Condition," *Ironmaking & Steelmaking*, Vol. Vol.29 (5), 2002, 326-336.
- [7]. G. Abbel, W. Damen, G. decendt, W. Tiekink, "Argon Bubbles in Slabs," *ISIJ*, Vol. 36, 1996, S219-S222.
- [8]. W.H. Emling, T.A. Waugaman, S.L. Feldbauer, A.W. Cramb, "Subsurface Mold Slag Entrainment in Ultra-Low Carbon Steels," in *Steelmaking Conference Proceedings*, Vol. 77, ISS, Warrendale, PA, (Chicago, IL), 1994, 371-379.
- [9]. L. Kiriha, H. Tosawa and K. Sorimachi, "Behavior of Alumina CLuster in Ultra Low Carbon Steel during Steelmaking Process," *CAMP-ISIJ*, Vol. 13, 2000, 120.
- [10]. B.G. Thomas, A. Denisov and H. Bai, "Behavior of Argon Bubbles during Continuous Casting of Steel," in *Steelmaking Conference Proceedings*, Vol. 80, ISS, Warrendale, PA., 1997, 375-384.
- [11]. J. Knoepke, M. Hubbard, J. Kelly, R. Kittridge, J. Lucas, "Pencil Blister Reduction at Inland Steel Company," in *Steelmaking Conference Proceedings*, Vol. 77, ISS, Warrendale, PA, 1994, 381-388.
- [12]. W. Damen, G. Abbel, H. Schulte, G. decendt, "The Influence of the Mould Process on Argon Bubbles in Slabs," 1996,
- [13]. L. Zhang, B.G. Thomas and B. Rietow, "Investigation of Ingot Inclusions Using Microscope and SEM . Univ. of Illinois at Urbana-Champaign. IMF project report.," Report No. CCC200406, University of Illinois at Urbana-Champaign, 2004.
- [14]. Y. Miki and S. Takeuchi, "Internal Defects of Continuous Casting Slabs Caused by Asymmetric Unbalanced Steel Flow in Mold," *ISIJ Int.*, Vol. 43 (10), 2003, 1548-1555.
- [15]. R. Gass, H. Knoepke, J. Moscoe, R. Shah, J. Beck, J. Dzierzawski, P.E. Ponikvar, "Conversion of Ispat Inland's No.1 Slab Caster to Vertical Bending," in *ISSTech2003 Conference Proceedings*, ISS, Warrandale, PA, 2003, 3-18.
- [16]. P. Rocabois, J.-N. Pontoire, V. Delville, I. Marolleau, "Different Slivers Type Observed in Solla Steel Plants and Improved Practice to Reduce Surface Defects on Cold Roll Sheet," in *ISSTech2003 Conference Proceedings*, ISS, Warrandale, PA, 2003, 995-1006.

- [17]. H. Yin and H.T. Tsai, "Application of Cathodoluminescence Microscopy (CLM) in Steel Research," in ISSTech2003 Conference Proceedings, ISS, Warrendale, PA, 2003, 217-226.
- [18]. H. Schubert, *Int. J. Miner. Process.*, Vol. 56, 1999, 257-276.
- [19]. A.G. Szekely, "The Removal of Solid Particles from Molten Aluminum in the Spinning Nozzle Inert Gas Flotation Process," *Metal. Trans. B*, Vol. 7B (3), 1976, 259-270.
- [20]. K. Okumura, M. Kitazawa, N. Hakamada, M. Hirasawa, M. Sano, K. Mori, "Rate of SiO₂ Inclusion Removal from Molten Copper to Slag Under Gas Injection Stirring Condition," *ISIJ Inter.*, Vol. 35 (7), 1995, 832-837.
- [21]. Y. Miki, B.G. Thomas, A. Denisov, Y. Shimada, "Model of Inclusion Removal During RH Degassing of Steel," *Iron and Steelmaker*, Vol. 24 (8), 1997, 31-38.
- [22]. Y. Ye and J.D. Miller, "The Significance of Bubble Particle Contact Time during Collision in the Analysis of Flotation Phenomena," *Int. J. Miner. Process.*, Vol. 25 (3-4), 1989, 199-219.
- [23]. H.J. Schulze, *Miner. Process. Extractive Metall. Rev.*, Vol. 5, 1989, 43-76.
- [24]. Y. Xie, S. Orsten and F. Oeters, "Behaviour of Bubbles at Gas Blowing Into Liquid Wood's Metal," *ISIJ Int.*, Vol. 32 (1), 1992, 66-75.
- [25]. R.M. Wellek, A.K. Agrawal and A.H.P. Skelland, "Shape of Liquid Drops Moving in Liquid Media," *A. I. Ch. E. Journal*, Vol. 12 (5), 1966, 854-862.
- [26]. Y. Sahai and R.I.L. Guthrie, "Hydrodynamics of Gas Stirred Melts. I.--Gas/Liquid Coupling," *Metal. Trans B*, Vol. 13B (2), 182, 193-202.
- [27]. H. Tokunaga, M. Iguchi and H. Tatemichi, "Turbulence structure of bottom-blowing bubbling jet in a molten Wood's metal bath," *Metall. Mater. Trans. B*, Vol. 30B (1), 1999, 61-66.
- [28]. M. Iguchi, H. Tokunaga and H. Tatemichi, "Bubble and liquid flow characteristics in a Wood's metal bath stirred by bottom helium gas injection," *Metall. Mater. Trans. B*, Vol. 28B (6), 1997, 1053-1061.
- [29]. M. Sevik and S.H. Park, "The splitting of drops and bubbles by turbulent fluid flow," *J. of Fluids Eng. Trans. AIME* (53-60), 1973,
- [30]. S. Yokoya, S. Takagi, K. Tada, M. Iguchi, K. Marukawa, S. Hara, "Swirling Flow Effect in Bottomless Immersion Nozzle on Bulk Flow in High Throughput Slab Continuous Casting Mold," *ISIJ Int.*, Vol. 41 (10), 2001, 1201-1207.
- [31]. S. Yokoya, S. Takagi, S. Ootani, M. Iguchi, K. Marukawa, "Swirling Flow Effect in Submerged Entry Nozzle on Bulk Flow in High Throughput Slab Continuous Casting Mold," *ISIJ Int.*, Vol. 41 (10), 2001, 1208-1214.
- [32]. S. Yokoya, S. Takagi, M. Kaneko, M. Iguchi, K. Marukawa, S. Hara, "Swirling Flow Effect in Off-center Immersion Nozzle on Bulk Flow in Billet Continuous Casting Mold," *ISIJ Int.*, Vol. 41 (10), 2001, 1215-1220.
- [33]. S. Yokoya, S. Takagi, M. Iguchi, K. Marukawa, S. Hara, "Swirling Flow Effect in Immersion Nozzle for Continuous Casting Process," *ISIJ Int.*, Vol. 41 (Supplement), 2001, S47-S51.
- [34]. FLUENT6.1-Mannual, Report, Fluent Inc., Lebanon, New Hampshire, 2003.
- [35]. FLUENT5.1, Report, Fluent Inc., Lebanon, New Hampshire, 2000.
- [36]. R. Clift, J.R. Grace and M.E. Weber, *Bubbles, Drops and Particles*, Academic Press, INC., New York, 1978.

- [37]. J. Aoki, L. Zhang and B.G. Thomas, "Modeling of Inclusion Removal in Ladle Refining," in The 3rd International Congress on the Science and Technology of Steelmaking, AIST, Warrendale, PA, 2005, In press.
- [38]. L. Zhang and B.G. Thomas, "Fluid Flow and Inclusion Motion in the Continuous Casting Strand," in Steelmaking National Symposium Mexico, (Morelia, Mich, Mexico), 2003.
- [39]. B.G. Thomas and L. Zhang, "Mathematical Modeling of Fluid Flow in Continuous Casting," *ISIJ Inter.*, Vol. 41 (10), 2001, 1181-1193.
- [40]. L. Zhang and B.G. Thomas, "Particle Motion with Random Walk Model in k-e Two-Equation Model Compared with LES Simulation," Report No. CCC200501, University of Illinois at Urbana-Champaign, 2005.
- [41]. Q. Yuan, B.G. Thomas and S.P. Vanka, "Study of Transient Flow and Particle Transport during Continuous Casting of Steel Slabs, Part 2. Particle Transport.," *Metal. & Material Trans. B.*, Vol. 35B (4), 2004, 703-714.
- [42]. M. Yemmou, M.A.A. Azouni and P. Casses, "Thermal Aspects of Particle Engulfment by a Solidifying Front," *J. Crystal Growth*, Vol. 128 (4), 1993, 1130-1136.
- [43]. J.K. Kim and P.K. RRRohatgi, "An Analysis Solution of the Critical Interface Velocity for the Encapturing of Insoluble Particles by a Moving Solid/Liquid Interface," *Metall. & Mater. Trans. B*, Vol. 29A (1), 1998, 351-375.
- [44]. D.M. Stefanescu and A.V. Catalina, "Note: Calculation of the critical velocity for the pusying/engulfment transition of nonmetallic inclusions in steel," *ISIJ Int.*, Vol. 38 (5), 1998, 503-505.
- [45]. B.G. Thomas, L. Zhang and T. Shi, "Effect of Argon Gas Distribution on FLuid Flow in the Mold Using Time-Averaged k-e Models," Report No. CCC200105, University of Illinois at Urbana-Champaign, 2001.
- [46]. H. Bai and B.G. Thomas, "Bubble Formation during Horizontal Gas Injection into Downward Flowing Liquid," *Metall. Mater. Trans. B*, Vol. 32B, 2001, 1143-1159.
- [47]. L. Zhang, B.G. Thomas, K. Cai, L. Zhu, J. Cui, "Inclusion Investigation during Clean Steel Production at Baosteel," in ISSTech2003, ISS, Warrendale, PA, 2003, 141-156.